Electronic Supplementary Material (ESI) for Nanoscale Advances.

Supporting Information

Metal Oxide Decorated Porous Carbons from Controlled Calcination of a Metal-Organic Framework

Gregory S. Day, Jialuo Li, Elizabeth A. Joseph, Peter Metz, Zachary Perry,
Matthew R. Ryder*, Katharine Page*, and Hong-Cai Zhou*

Experimental Section

All chemicals used in this study were used as received without further purification. The PCN-250 was provided by *framergy*, Inc. and used without further purification. The TGA measurements were performed on a Mettler-Toledo TGA/DSC 1 equipped with a GC 200 Gas controller system. D_2O saturated TGA experiments were performed using a water tank and flowing the gas (N_2) over the water, leading to a saturated gas stream, 2% by volume at room temperature, as confirmed by connecting a mass spectrometer to the TGA. All N_2 adsorption measurements were performed on a Micromeritics BET 2420 instrument at 77K. SEM images were collected using an FEI Quanta 600 FE-SEM. PXRD data were collected with a Bruker-AXS D8 short arm diffractometer equipped with a multiwire lynx eye detector using Cu (Kα, λ=1.542Å). It was operated at a potential of 40 kV and a current of 40 mA. Variable temperature PXRD was performed on a Bruker D8 Advance short arm diffractometer equipped with a multiwire lynx eye detector and an MTC oven capable of going from room temperature to 1000 °C. The oven chamber was fitted with an inert gas purge for experiments under N_2, He, or Ar. Elemental Analysis was performed at Atlantic Microlab, Inc, using combustion analysis. The neutron diffraction data were acquired using the nanoscale ordered materials diffractometer (NOMAD) at the Spallation Neutron Source (SNS) at Oak Ridge National Laboratory (ORNL).[1] The data was collected using ~100 mg of material placed within a 2 mm quartz capillary. Rietveld refinement of the Bragg diffraction peaks for both the neutron and x-ray data was performed using the GSAS-II program.[2] Pair distribution function analysis (PDF) of the neutron total scattering data was conducted using PDFGui.[3]

Synthesis of MOF-Derived Carbons

PCN-250 (900 mg) was placed into a 7 mL ceramic crucible and loaded into a quartz tube. The quartz tube was placed in a tube furnace and had one end attached to a gas line. The tube was purged with the gas being studied for 15 minutes before heating was started. The quartz tube was then heated at a ramp rate of 5 °C/min to 500 °C, wherein it was held for 4 hours. After cooling to room temperature, the synthesis gas was turned off, and the MOF-derived carbons were unloaded into glass vials in air and analyzed as collected. The D_2O calcination was conducted using a similar bubbler purge setup, as described for the TGA experiments.

Collection of Air Free Calcined Samples

PCN-250 (2.0 g) was loaded into a 3/4” stainless steel tube, which was attached via 1/8” stainless steel tubing to a set of 1/4” stainless steel tubing with a valve that was attached to the purge gas. The other end of the 3/4” tubing was left open to allow the gas to purge through. The gas was run through at 1 SLPM for 15 minutes before the tube furnace was heated to 500 °C and held there for 4 hours. After cooling to room temperature, the tube was sealed while still under gas flow and transferred into a glovebox. The sample was analyzed via PXRD using an air-free cell.

Table S1: Elemental Analysis of PCN-250 calcined at 500 °C under various conditions.

Atmosphere	C (wt%)	H (wt%)	N (wt%)
Air	0.15	0.0	0.0
H_2	7.50	0.60	1.04
D_2O	31.61	1.91	5.28
CO_2	16.65	0.73	3.08
N_2	24.25	1.47	3.62
He	30.24	1.25	3.09

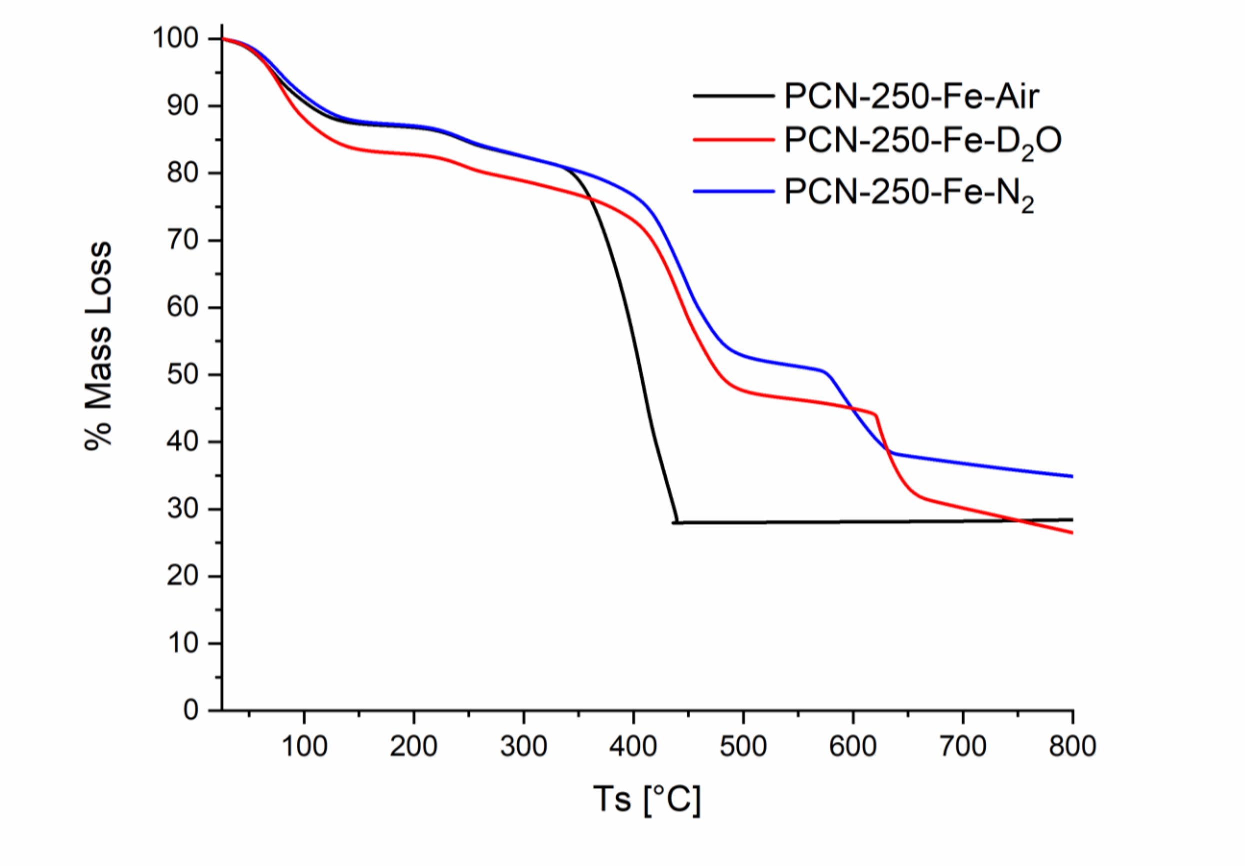

Figure S1: TGA curve of PCN-250 performed under a flow of air (black) water (D_2O) enriched N_2 (red) and N_2 (blue)

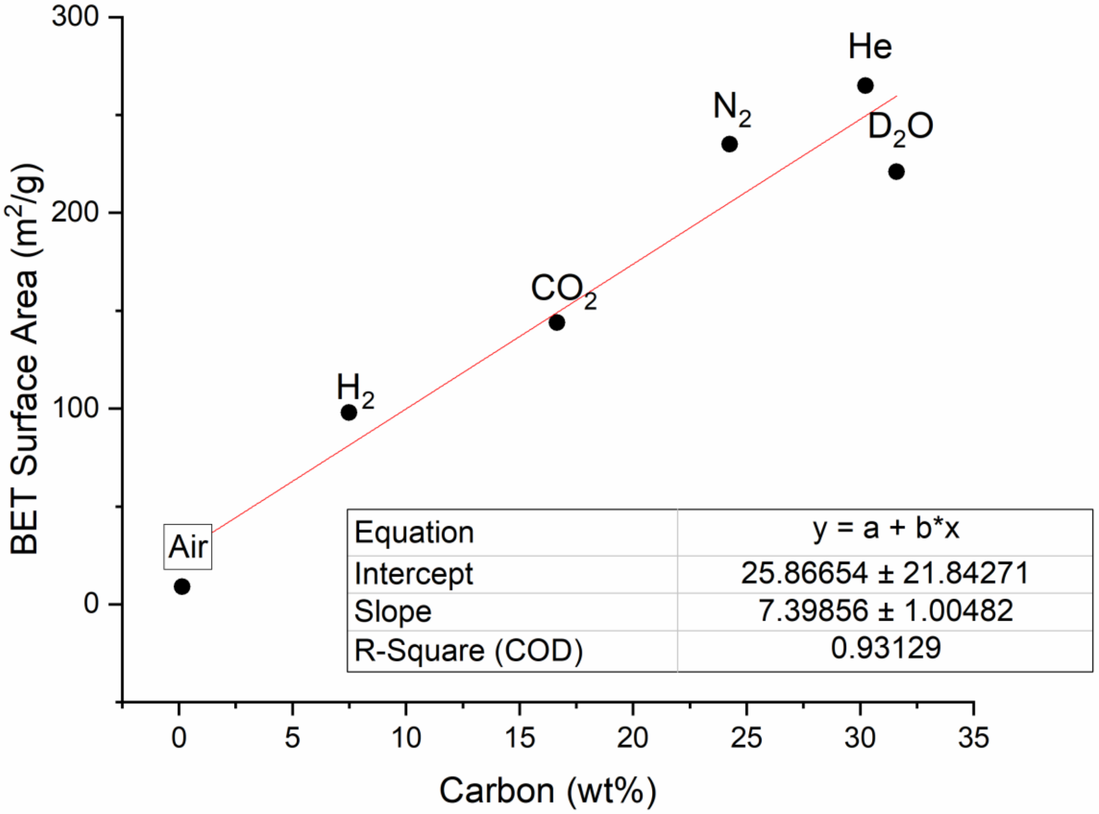

Figure S2: BET Surface area versus the residual carbon content of the MOF derived carbons, showing an excellent linear correlation between the two parameters.

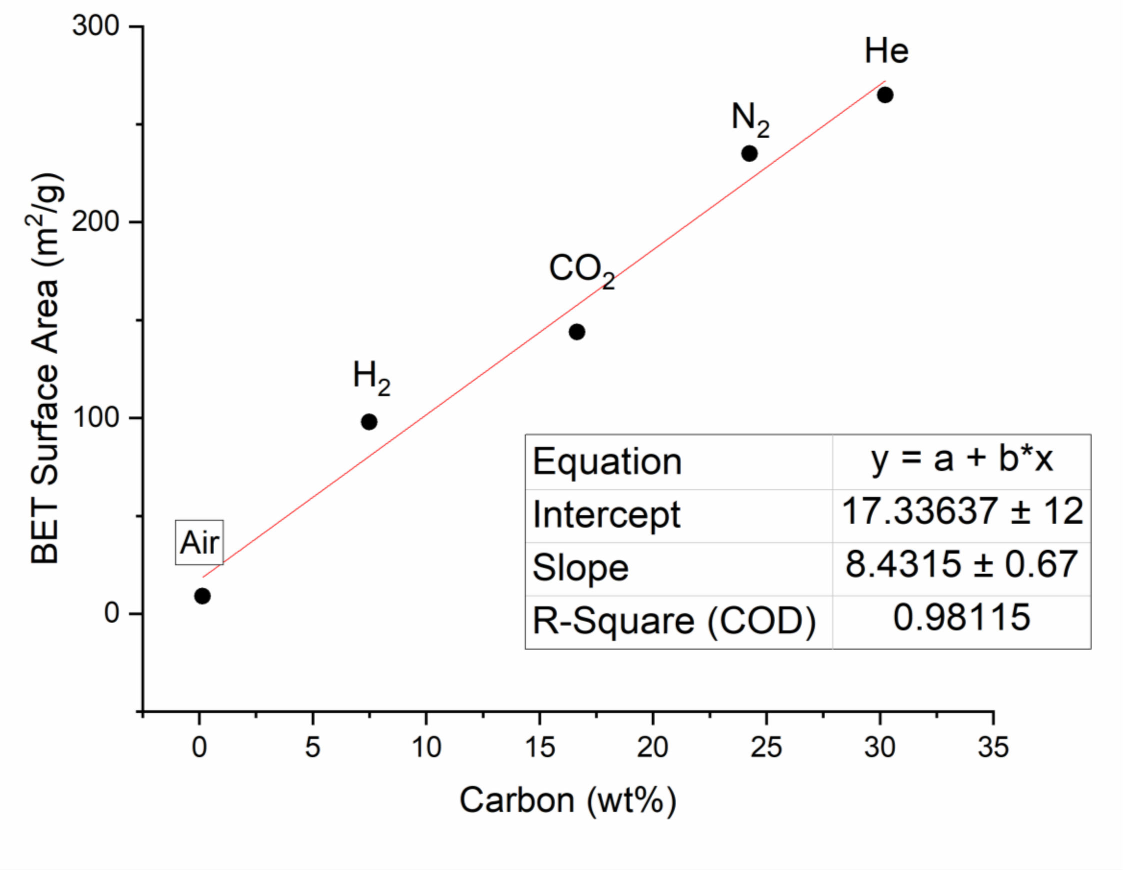

Figure S3: BET Surface area versus the residual carbon content of the MOF derived carbons with the D_2O calcined sample being excluded, exhibiting a higher degree of correlation amongst the data points.

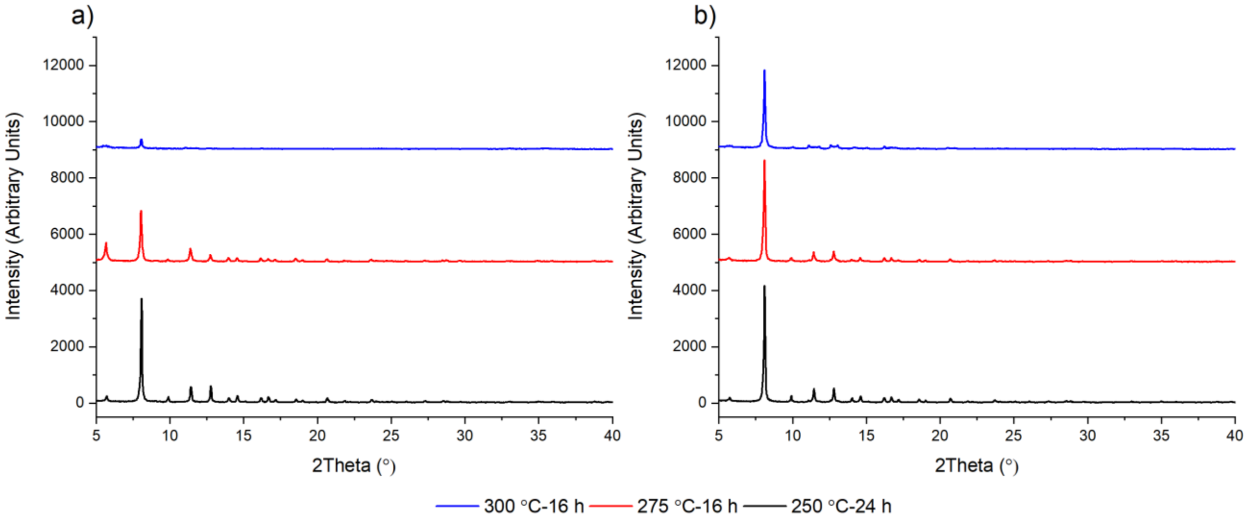

Figure S4: PXRD patterns for PCN-250 calcined at low temperatures under a) water and b) N_2. The heating temperatures and times were kept consistent between the two sets of samples.

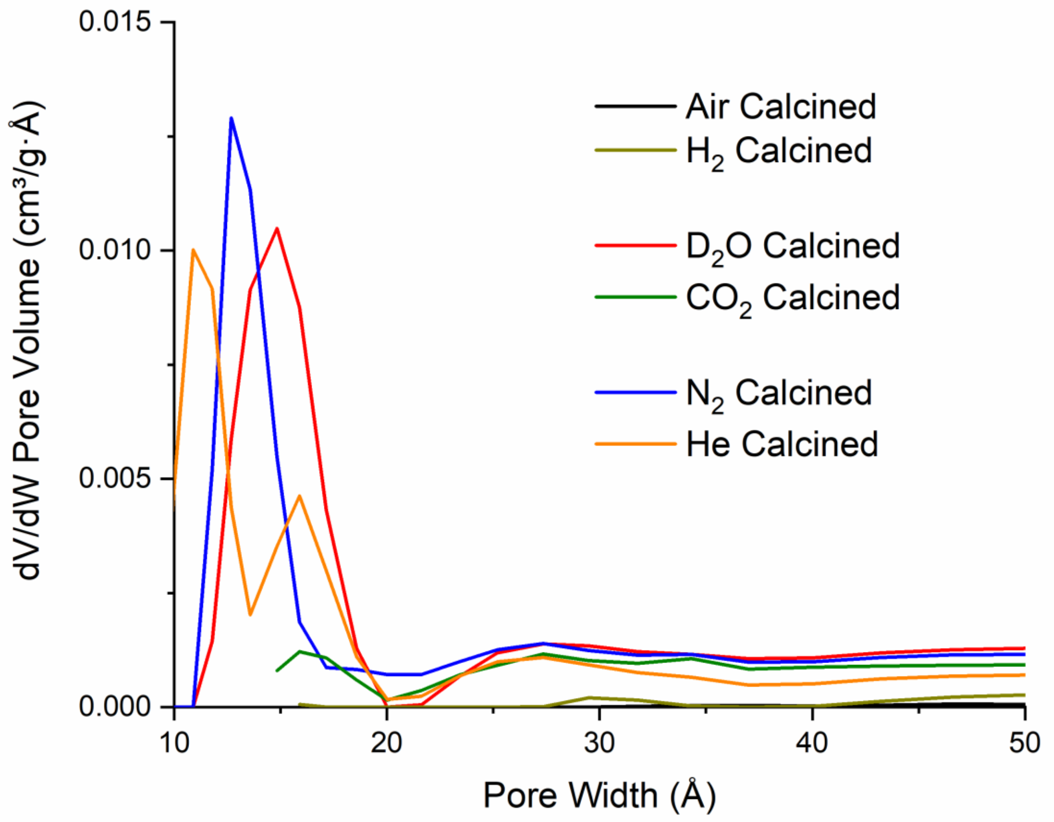

Figure S5: BJH Pore size distribution data for the PCN-250-derived carbons showing a change in the degree of mesoporosity between the different samples.

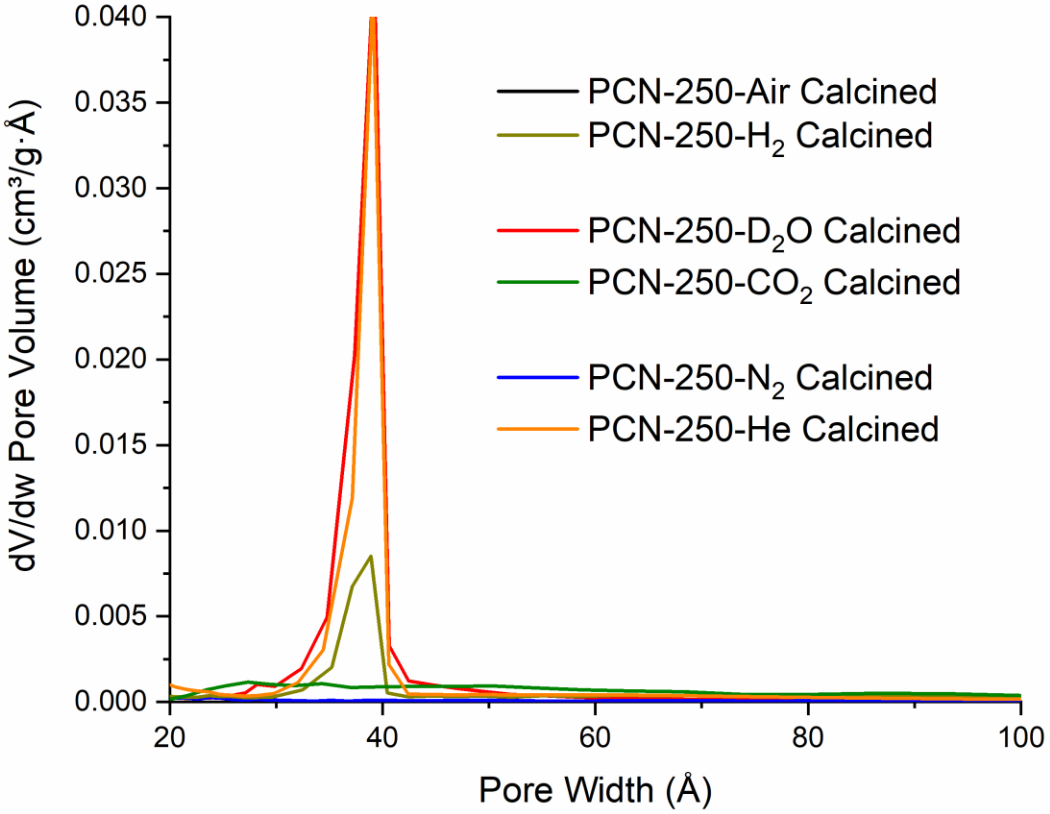

Figure S6: DFT Pore size distribution of the PCN-250-derived carbons. Only the D_2O in N_2, N_2, and He calcined samples show significant levels of microporosity remaining.

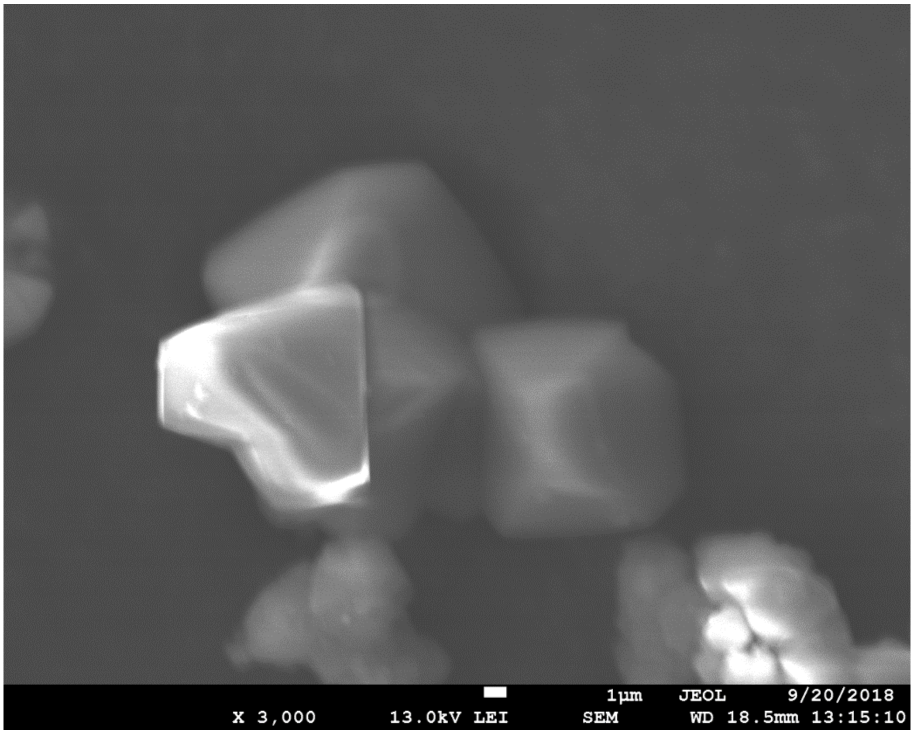

Figure S7: SEM of the as-synthesized PCN-250.

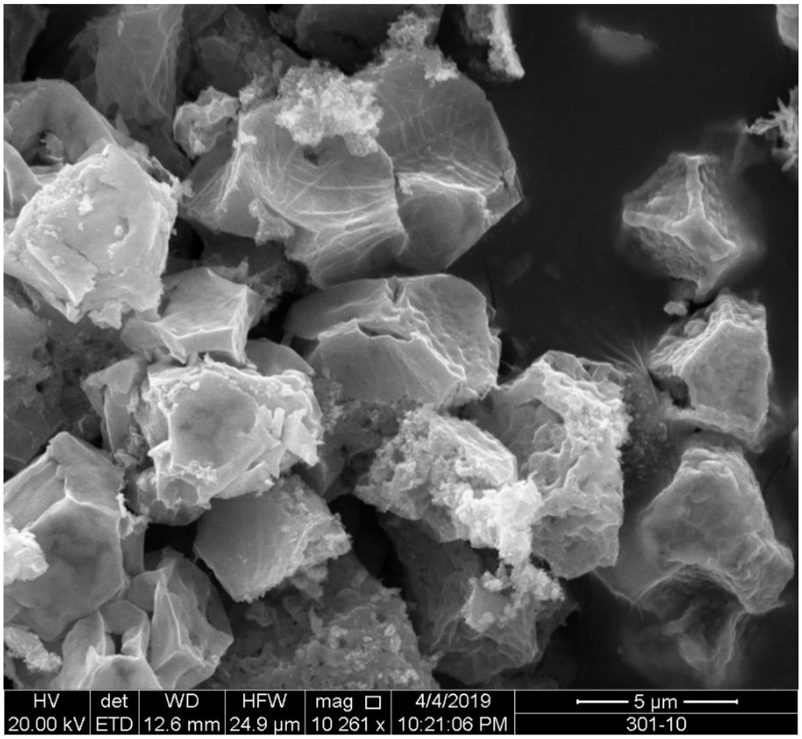

Figure S8: SEM of the air calcined PCN-250.

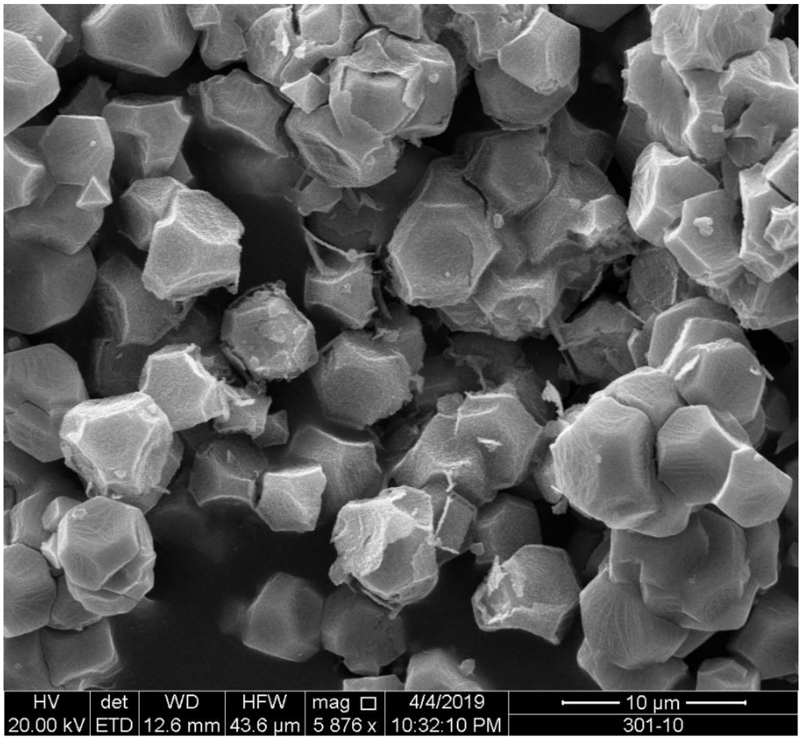

Figure S9: SEM of the H_2 calcined PCN-250.

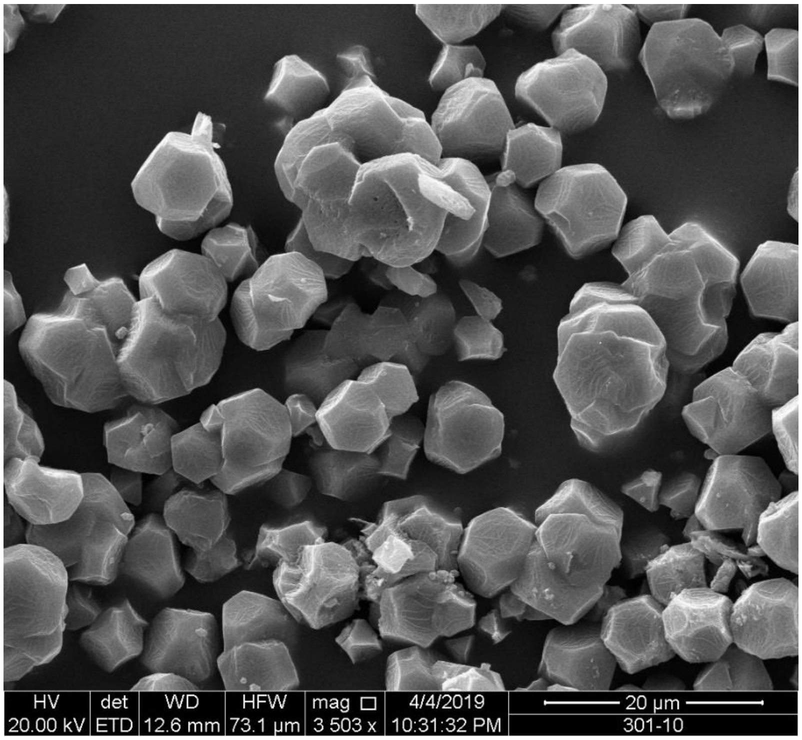

Figure S10: SEM of the D_2O calcined PCN-250.

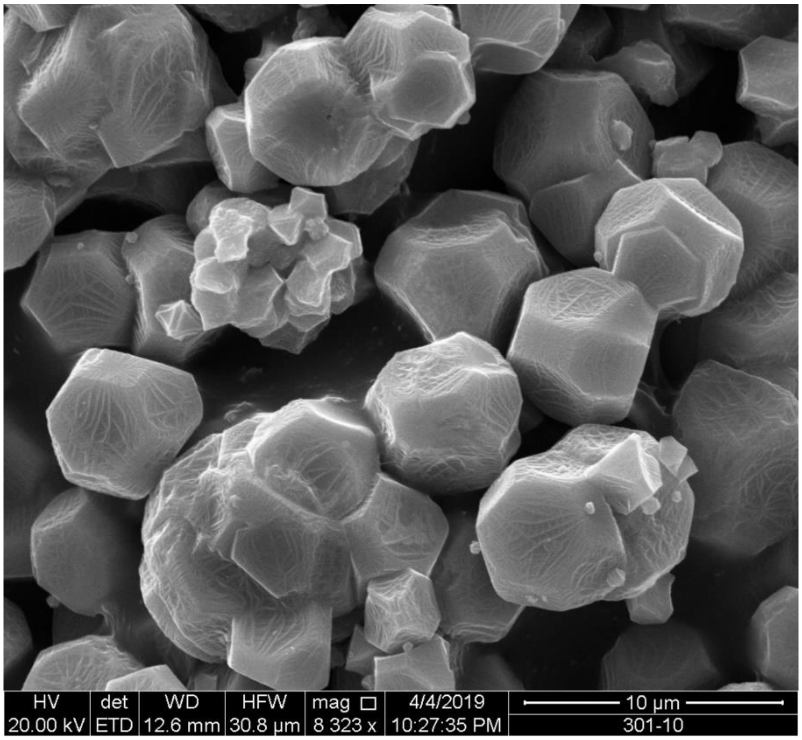

Figure S11: SEM of the CO_2 calcined PCN-250.

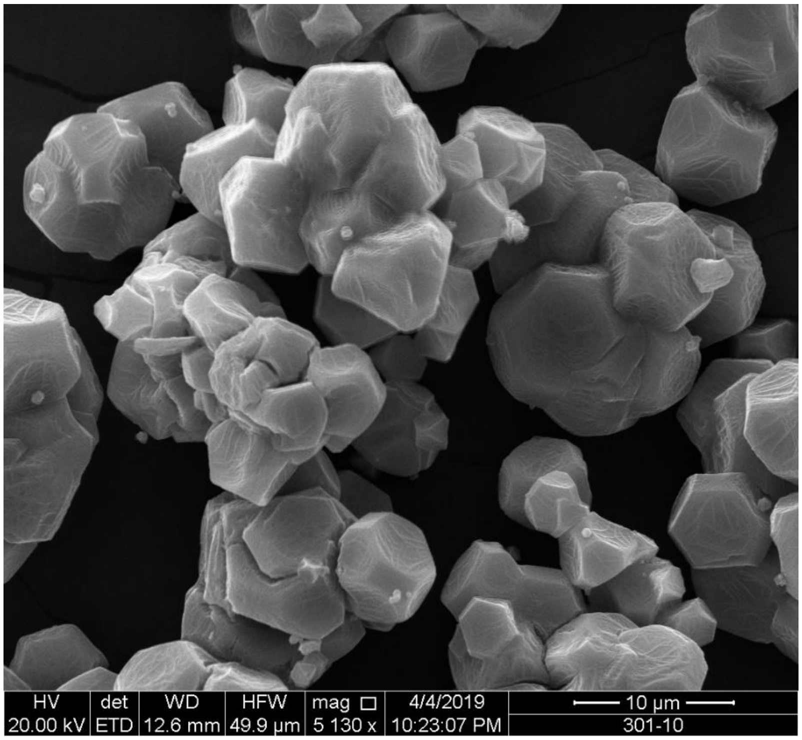

Figure S12: SEM of the N_2 calcined PCN-250.

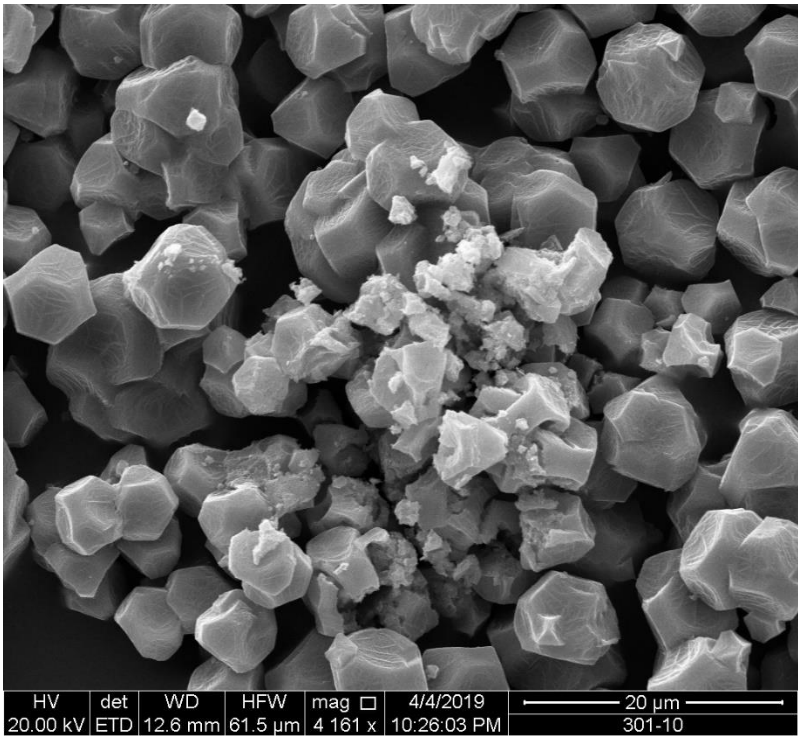

Figure S13: SEM the He calcined PCN-250.

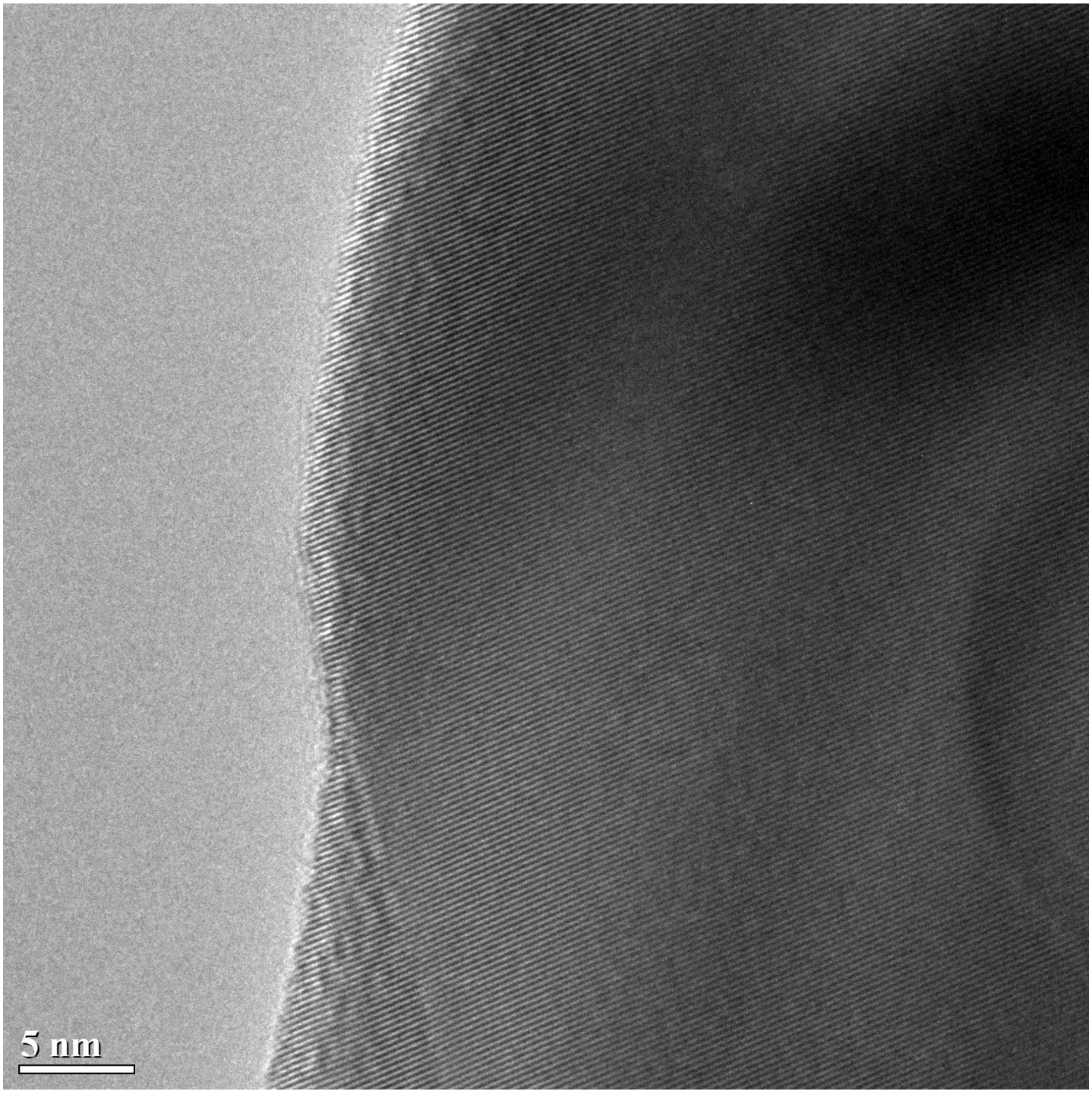

Figure S14: TEM of PCN-250 calcined under air.

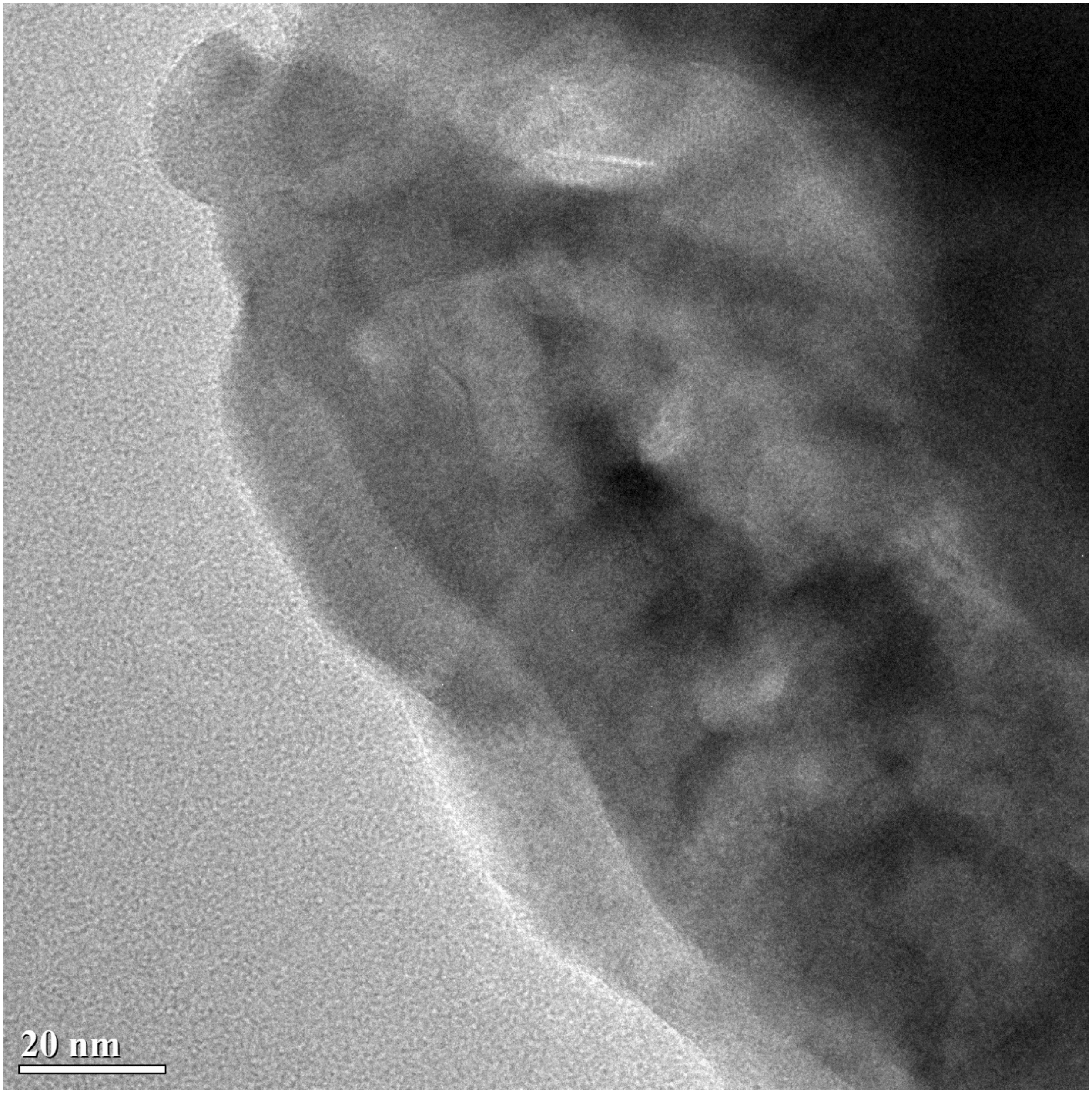

Figure S15: TEM of PCN-250 calcined under H_2.

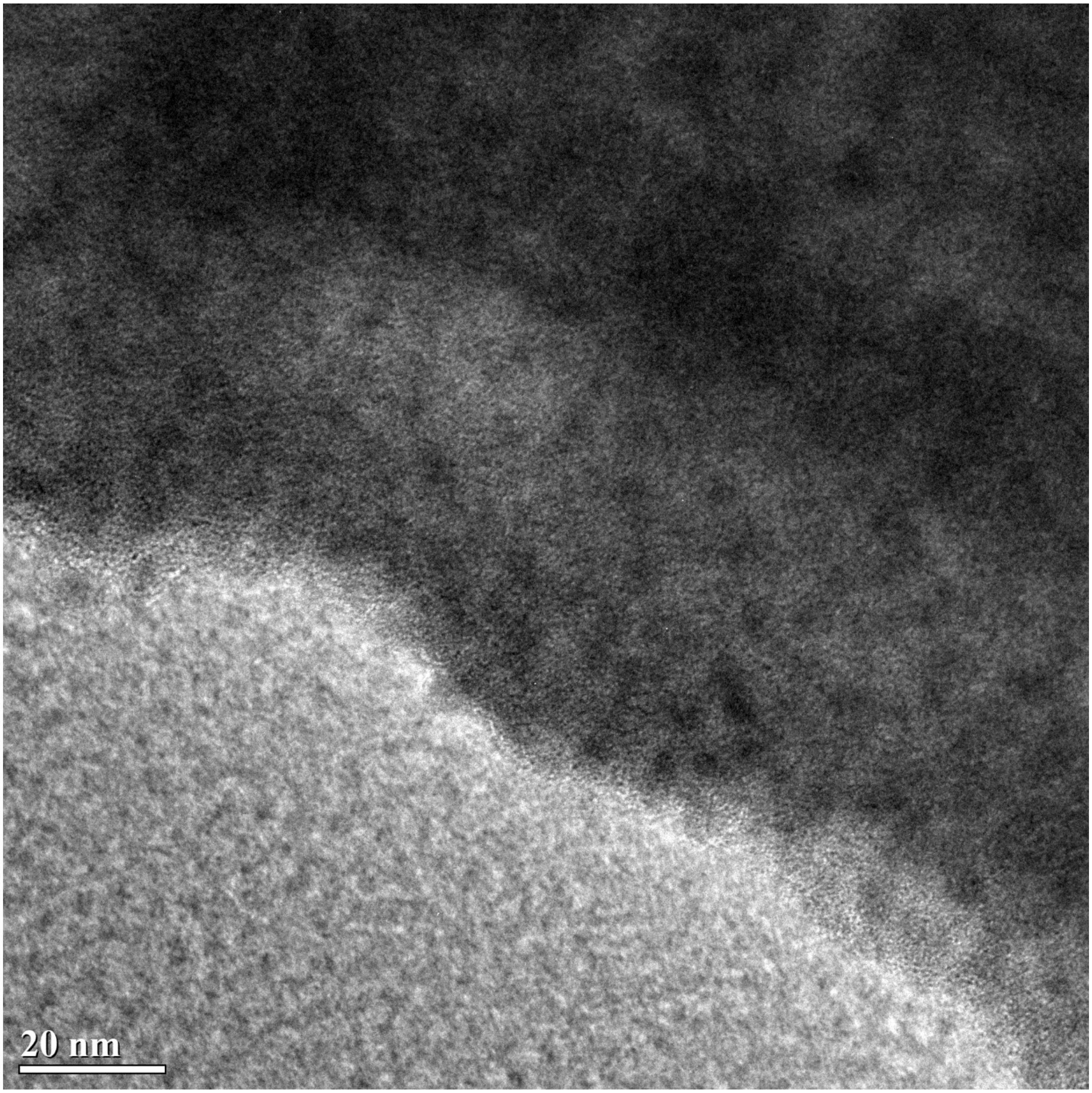

Figure S16: TEM of PCN-250 calcined under D_2O.

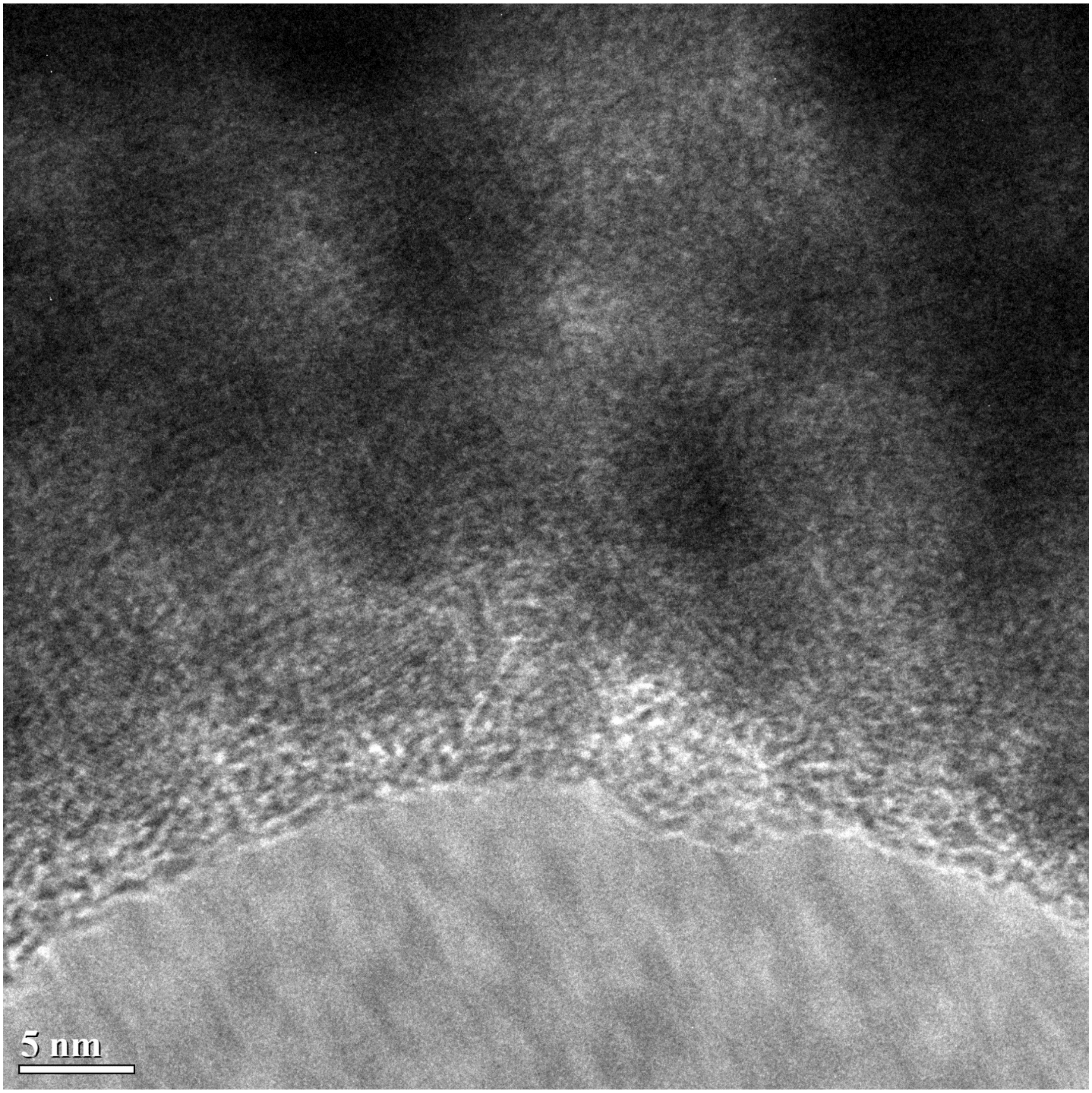

Figure S17: TEM of PCN-250 calcined under CO_2.

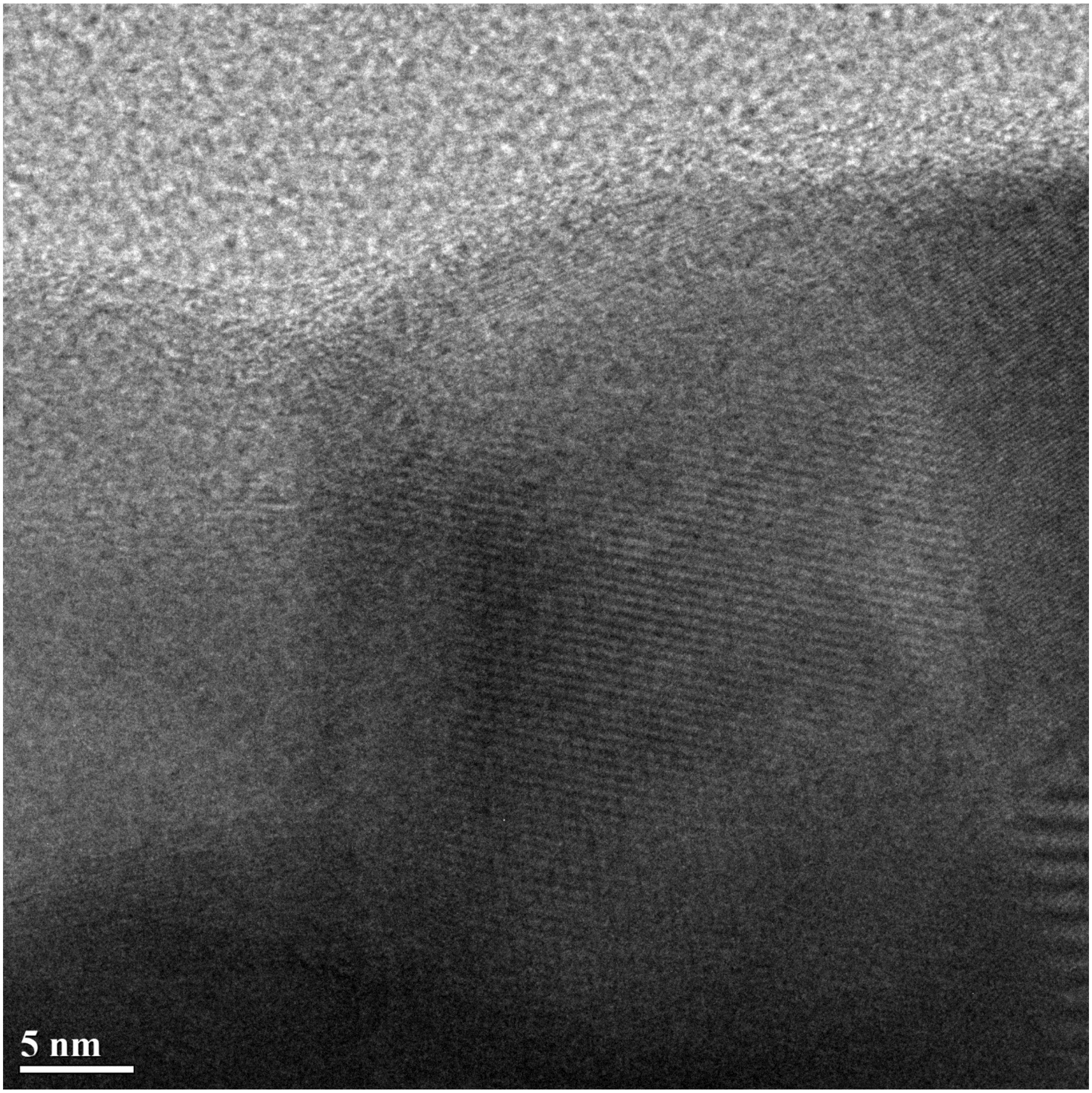

Figure S18: TEM of PCN-250 calcined under N_2 showing bulk iron oxide particles.

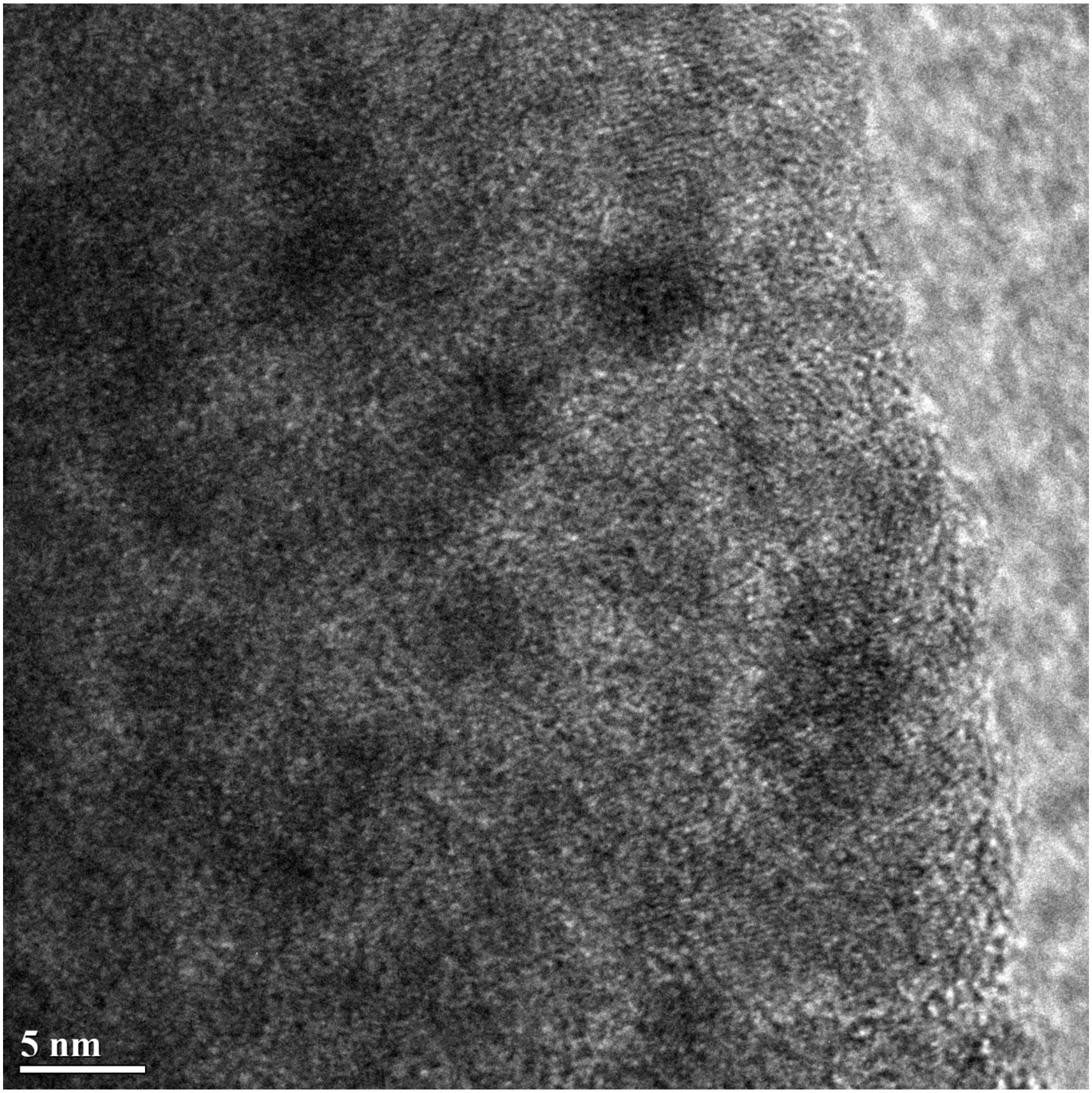

Figure S19: TEM of PCN-250 calcined under N_2 showing nanoscale iron oxide particles.

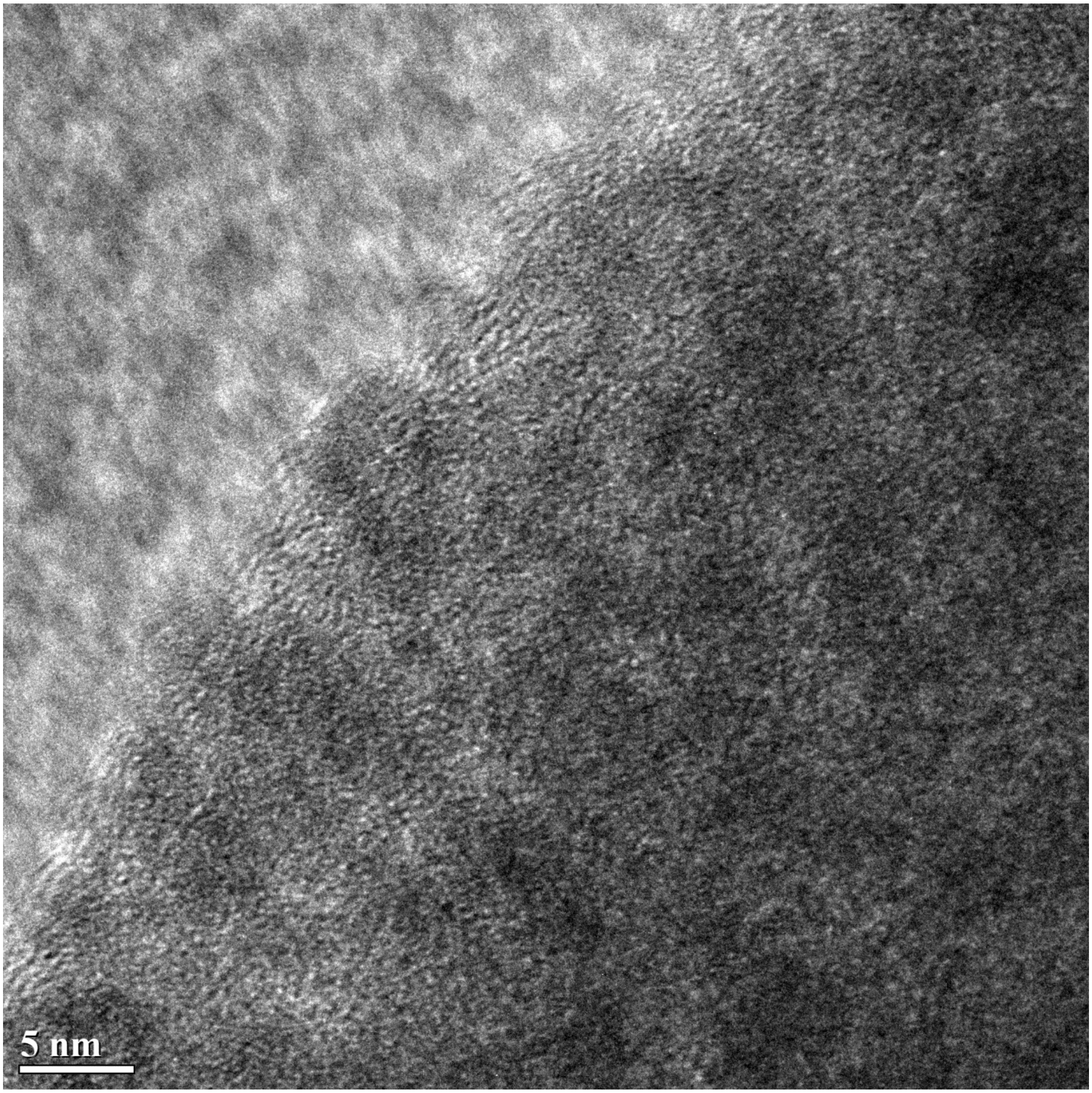

Figure S20: TEM of PCN-250 calcined under He.

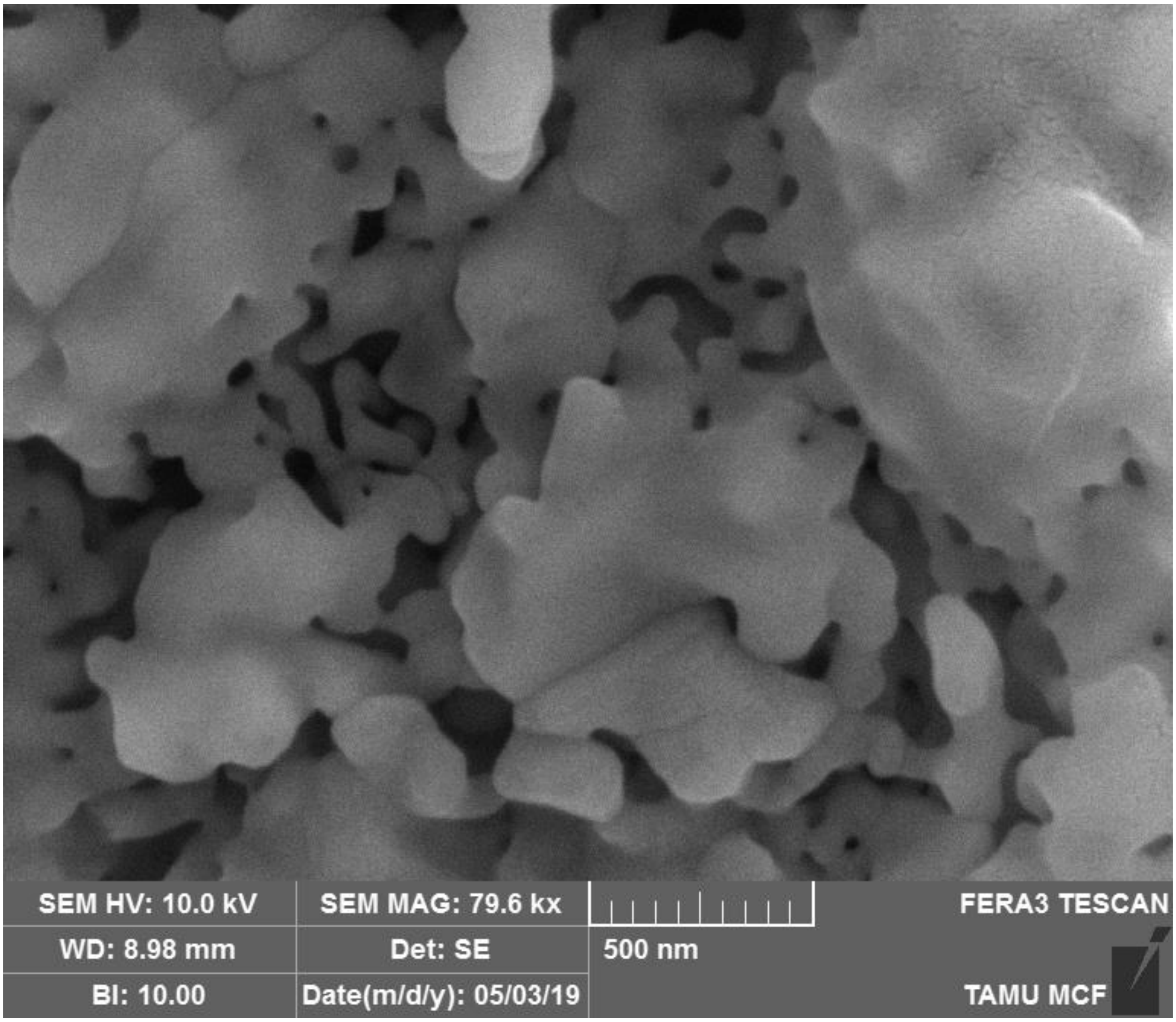

Figure S21: High-resolution SEM of the air calcined PCN-250 showing nanoscale porous features.

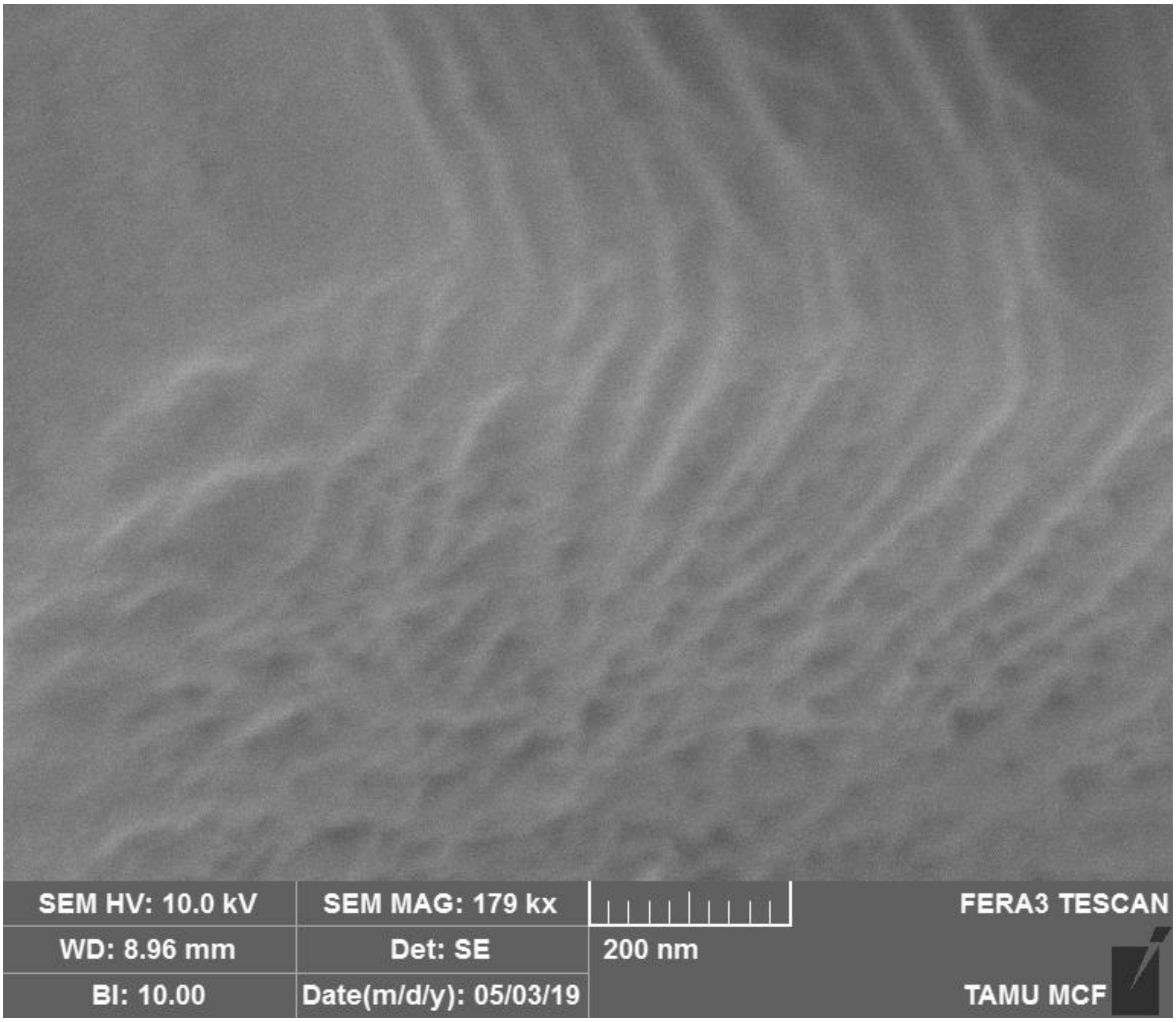

Figure S22: High-resolution SEM image of H_2 calcined PCN-250 showing nanoscale nodules as part of the surface wave pattern observed a lower magnification.

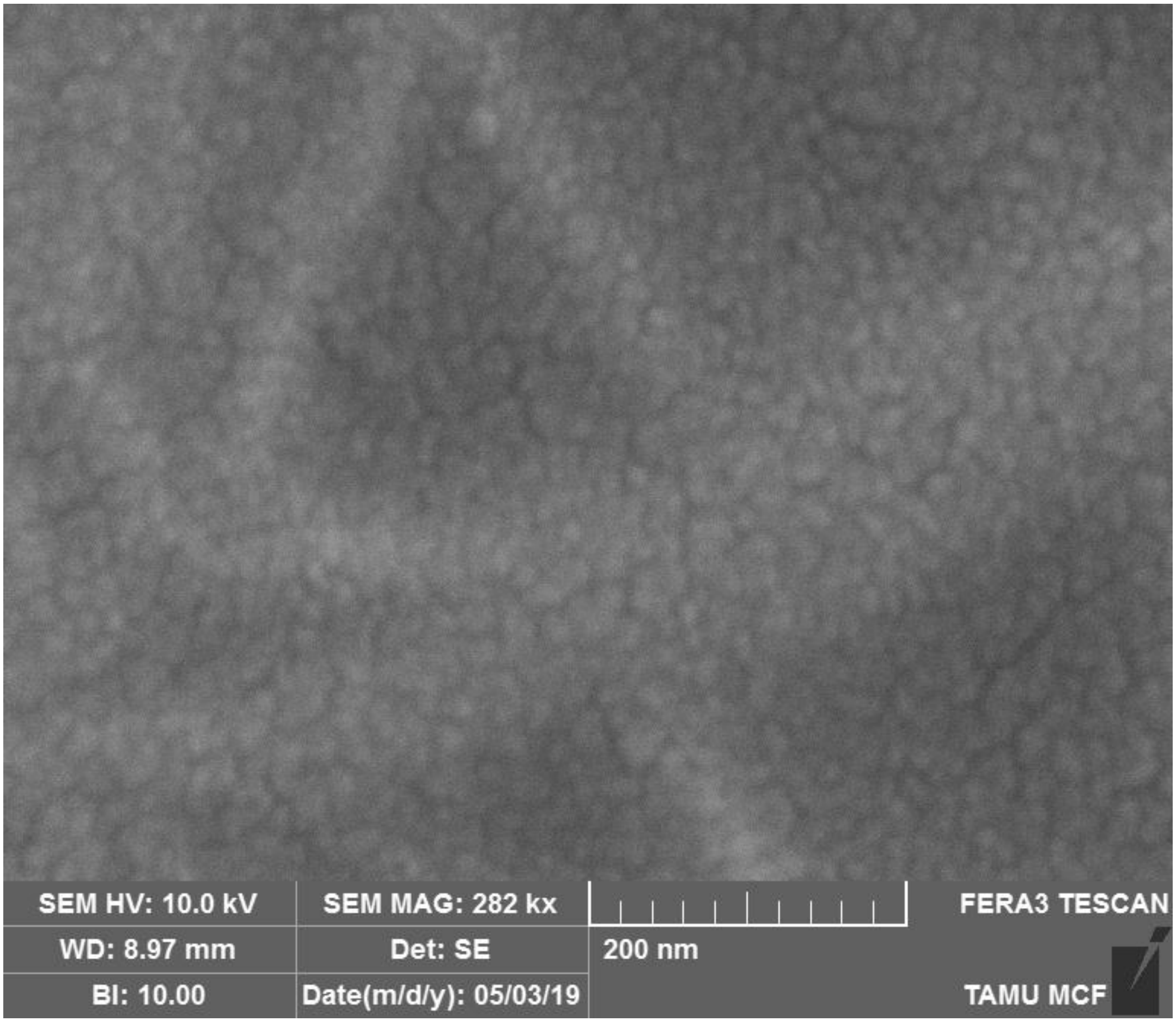

Figure S23: High-resolution SEM image of D_2O calcined PCN-250 showing nanoscale nodules.

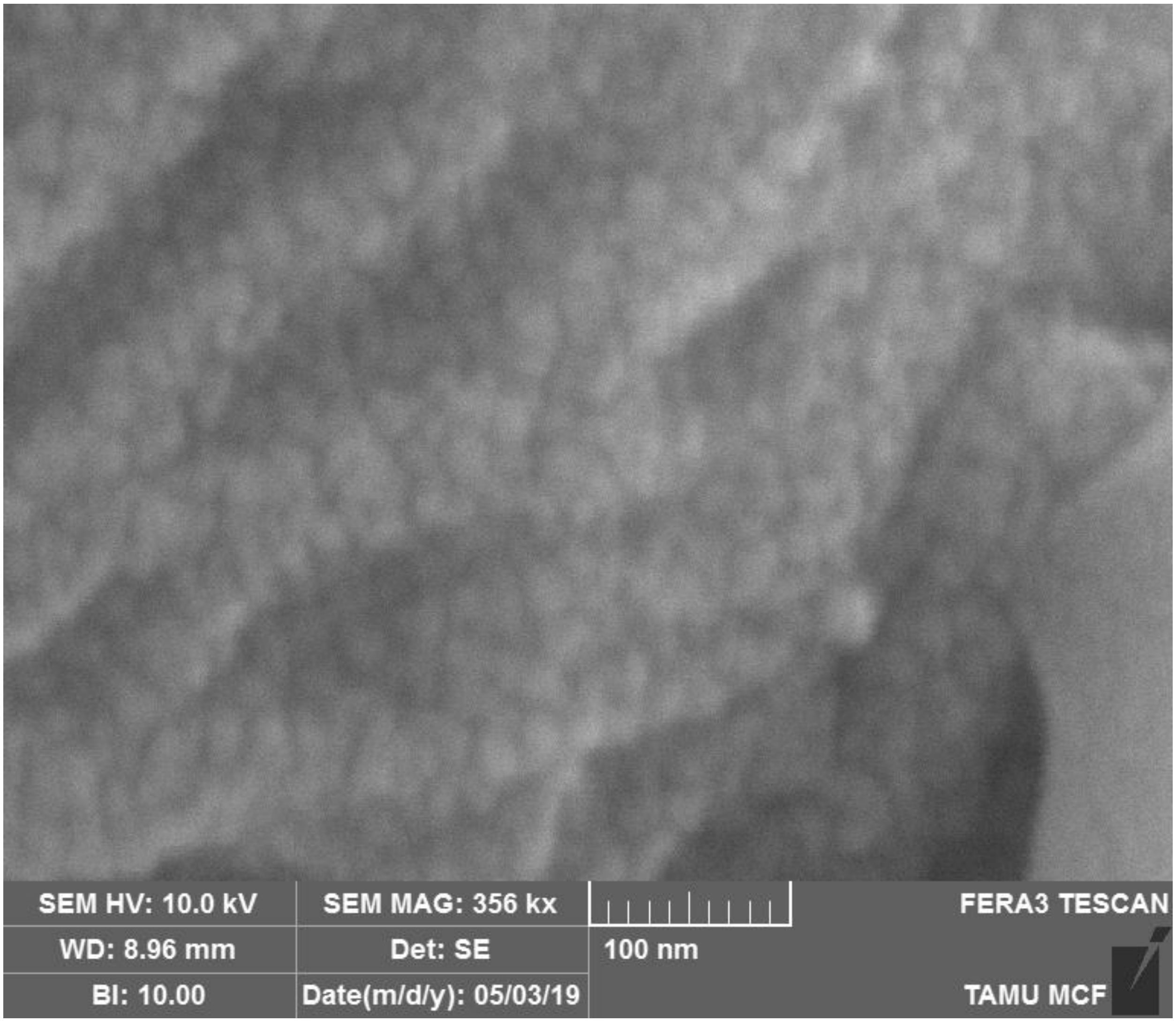

Figure S24: High-resolution SEM image of CO_2 calcined PCN-250 showing nanoscale nodules.

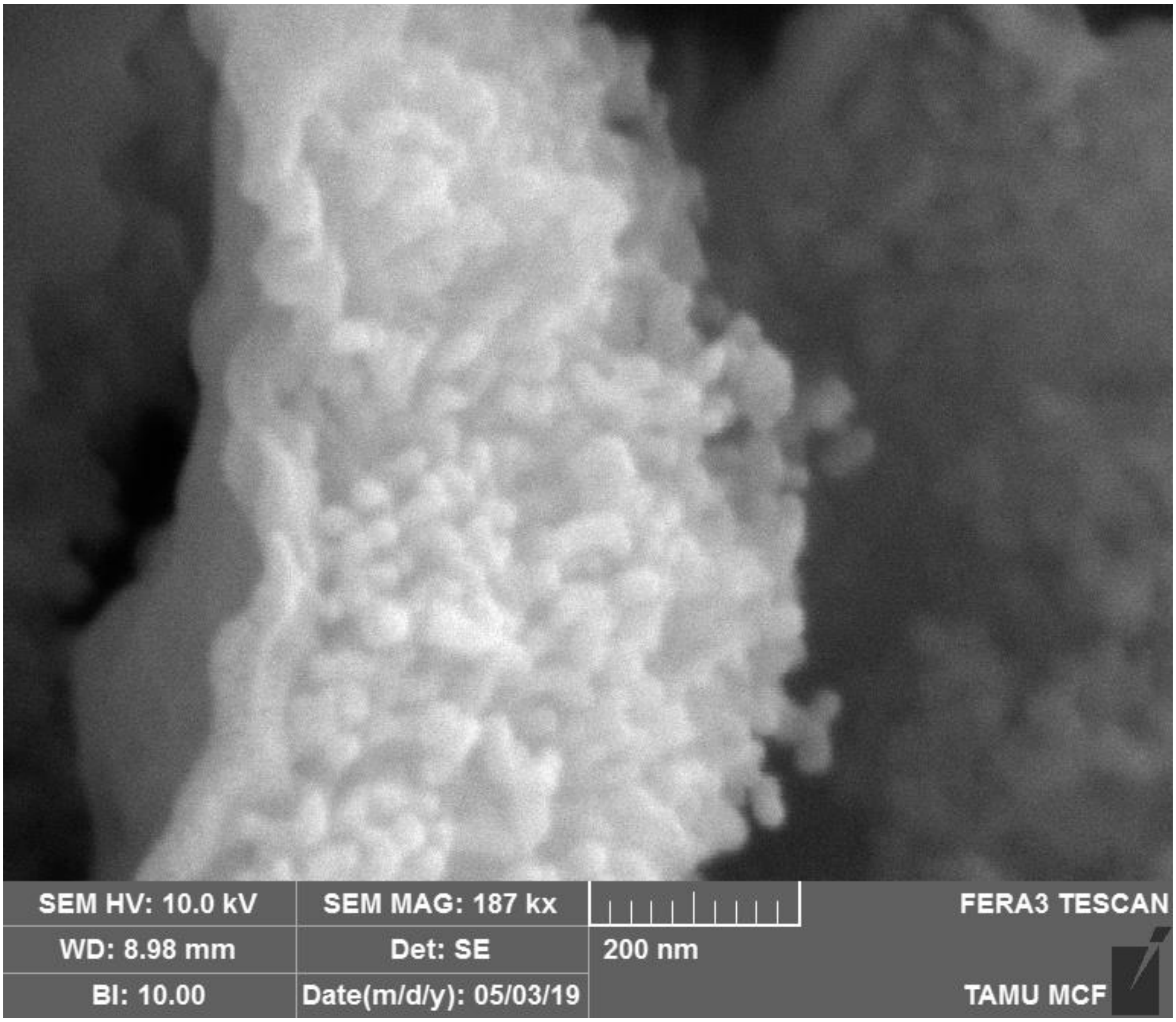

Figure S25: High-resolution SEM image of N_2 calcined PCN-250 showing nanoscale nodules.

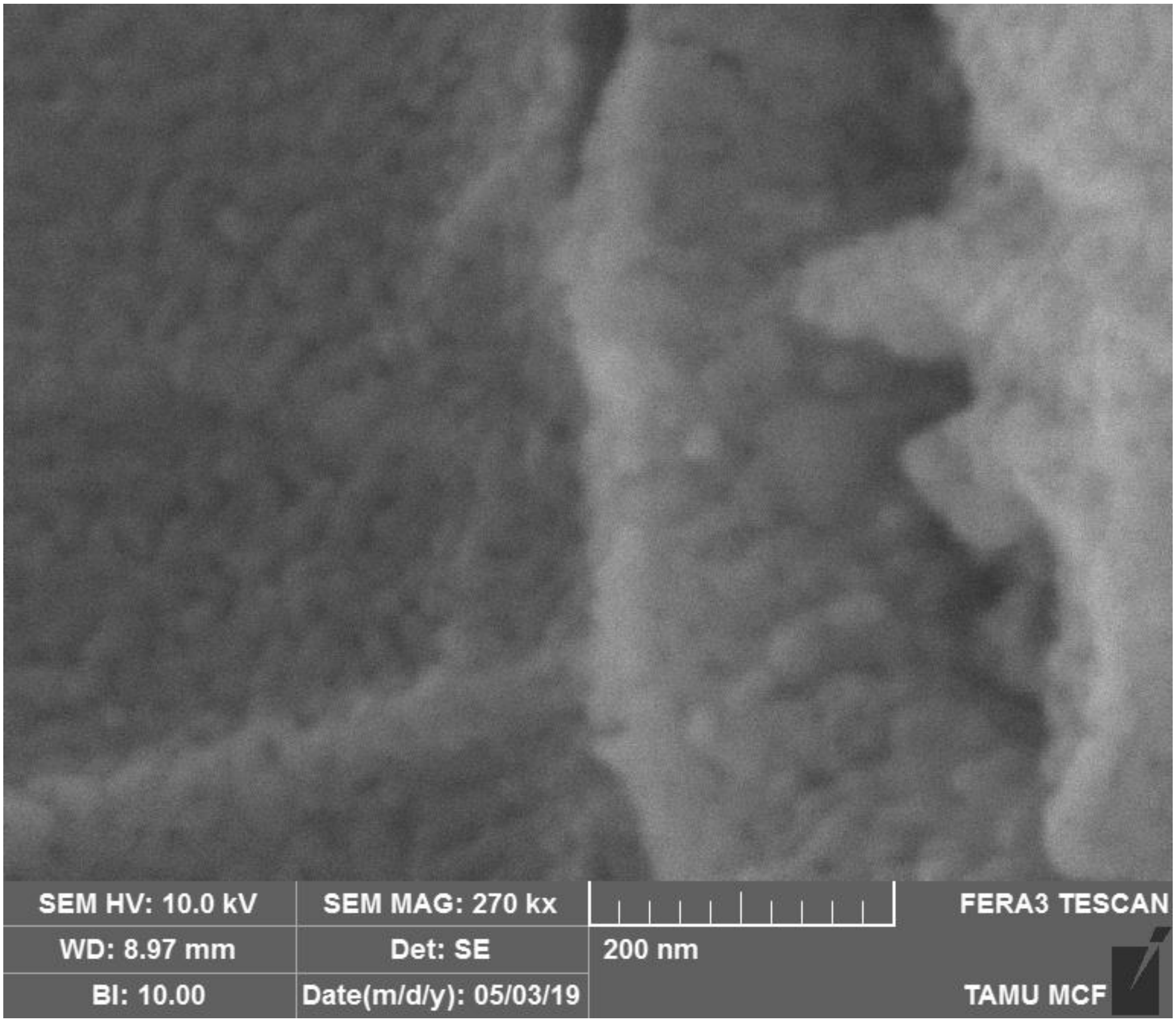

Figure S26: High-resolution SEM image of He calcined PCN-250 showing nanoscale nodules.

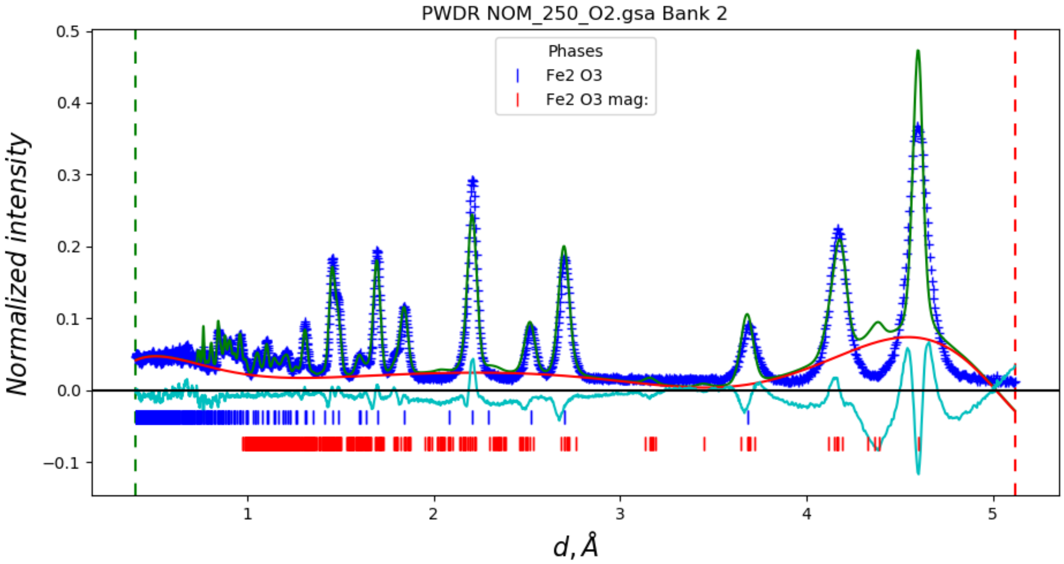

Figure S27: NOMAD bank 2 Rietveld refinement of the neutron Bragg peaks for air calcined PCN-250, containing both magnetic and nuclear components.

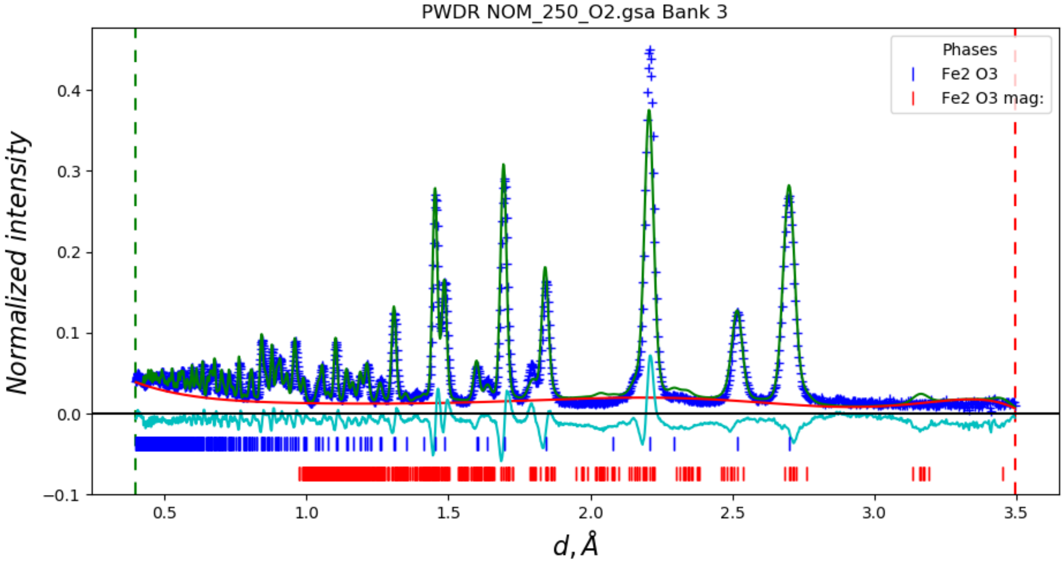

Figure S28: NOMAD bank 3 Rietveld refinement of the neutron Bragg peaks for air calcined PCN-250, containing both magnetic and nuclear components.

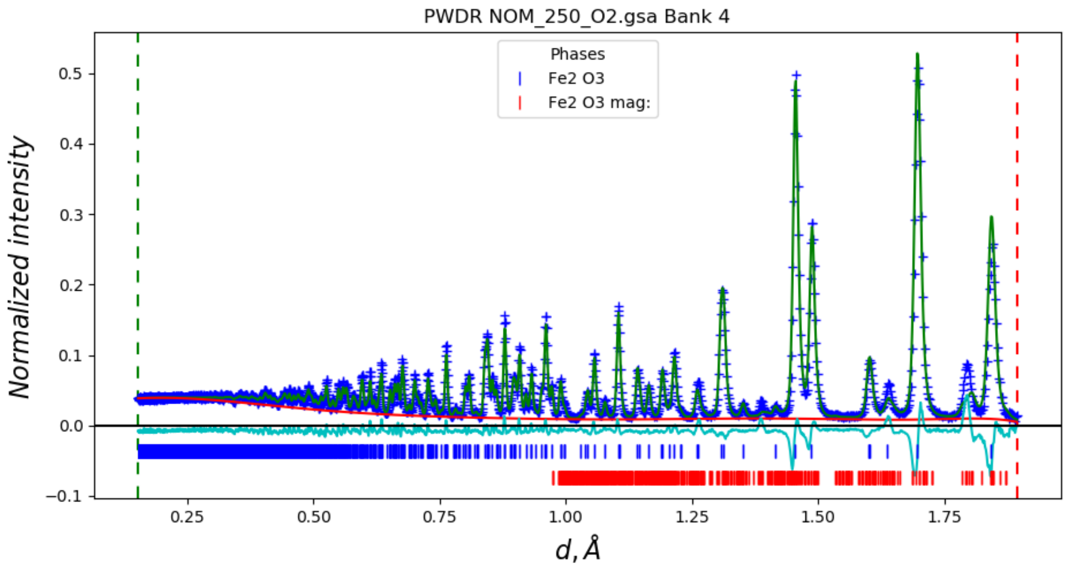

Figure S29: NOMAD bank 4 Rietveld refinement of the neutron Bragg peaks for air calcined PCN-250, containing both magnetic and nuclear components.

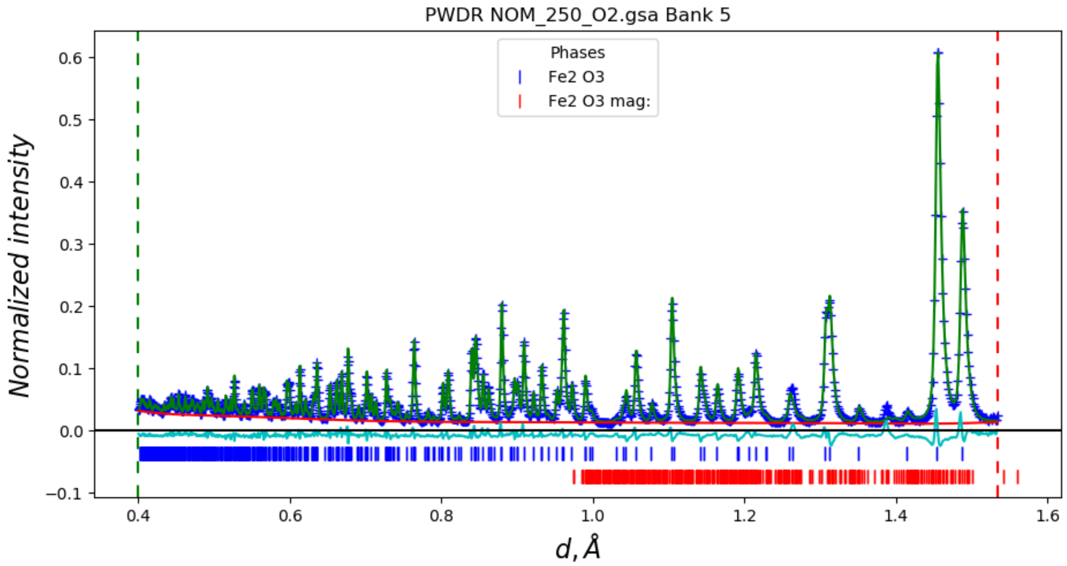

Figure S30: NOMAD bank 5 Rietveld refinement of the neutron Bragg peaks for air calcined PCN-250, containing both magnetic and nuclear components.

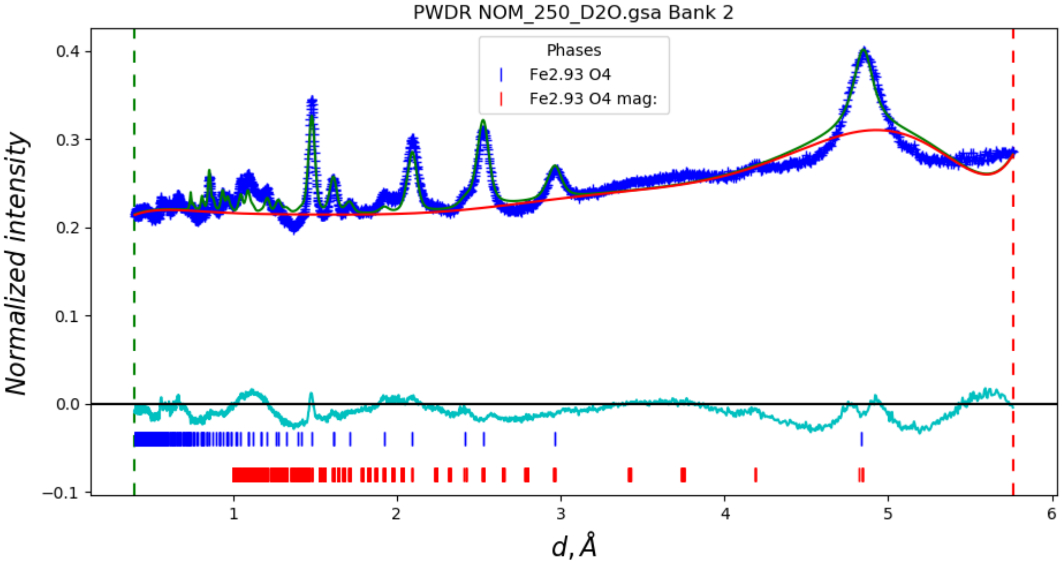

Figure S31: NOMAD bank 2 Rietveld refinement of the neutron Bragg peaks for D_2O calcined PCN-250, containing both magnetic and nuclear components.

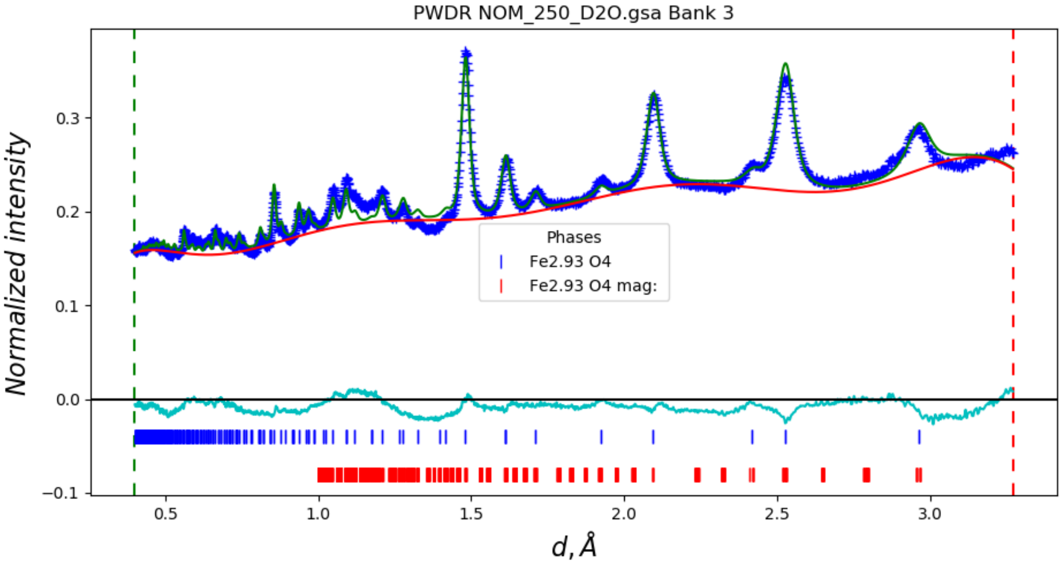

Figure S32: NOMAD bank 3 Rietveld refinement of the neutron Bragg peaks for D_2O calcined PCN-250, containing both magnetic and nuclear components.

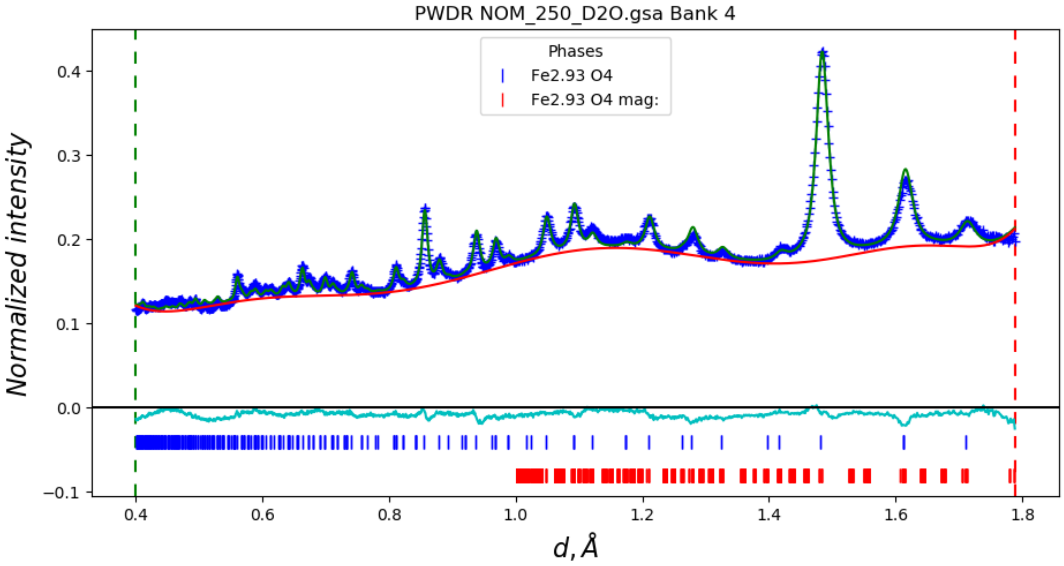

Figure S33: NOMAD bank 4 Rietveld refinement of the neutron Bragg peaks for D_2O calcined PCN-250, containing both magnetic and nuclear components.

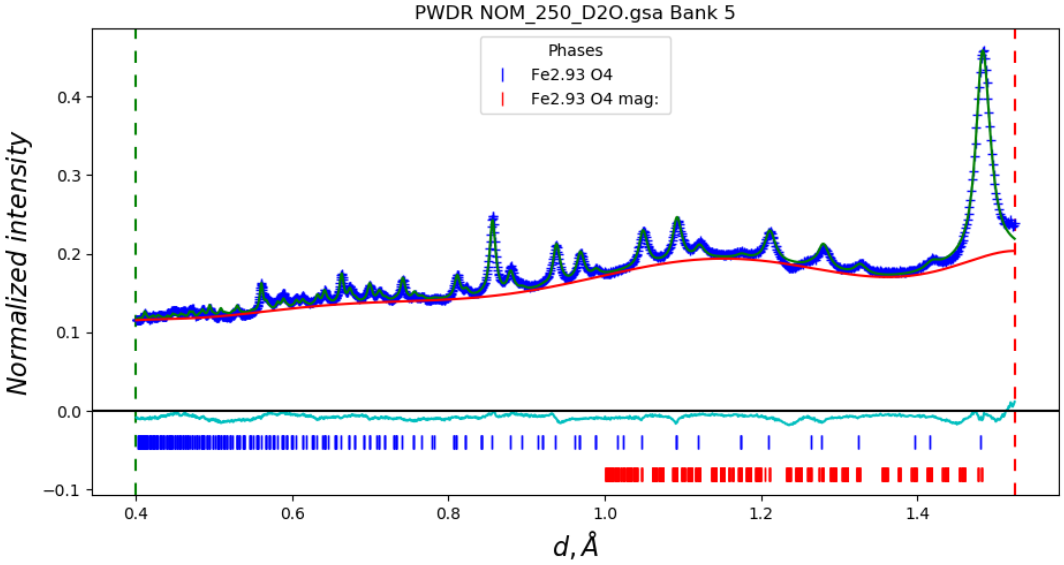

Figure S34: NOMAD bank 5 Rietveld refinement of the neutron Bragg peaks for D_2O calcined PCN-250, containing both magnetic and nuclear components.

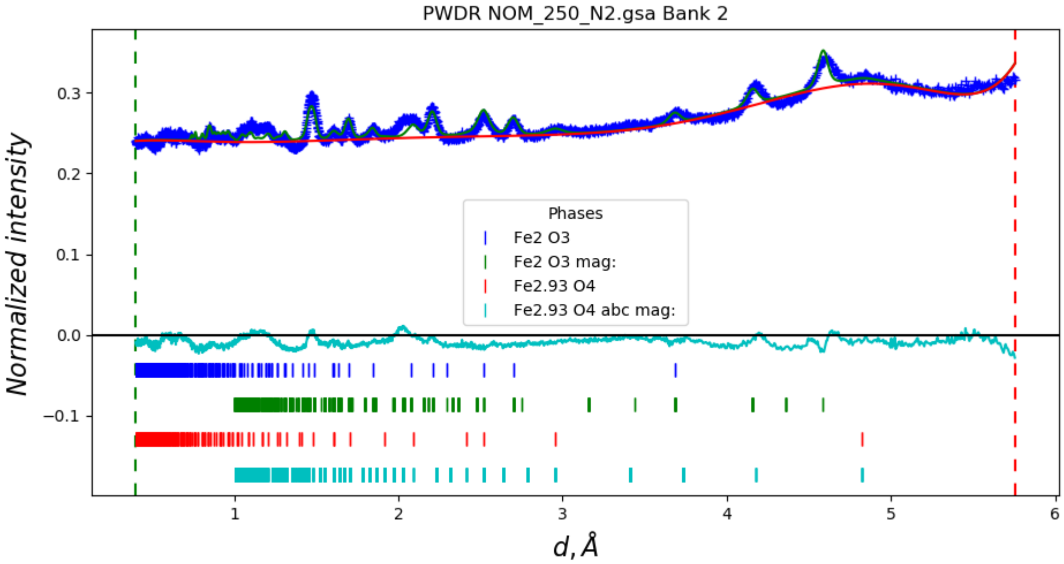

Figure S35: NOMAD bank 2 Rietveld refinement of the neutron Bragg peaks for N_2 calcined PCN-250, containing both magnetic and nuclear components.

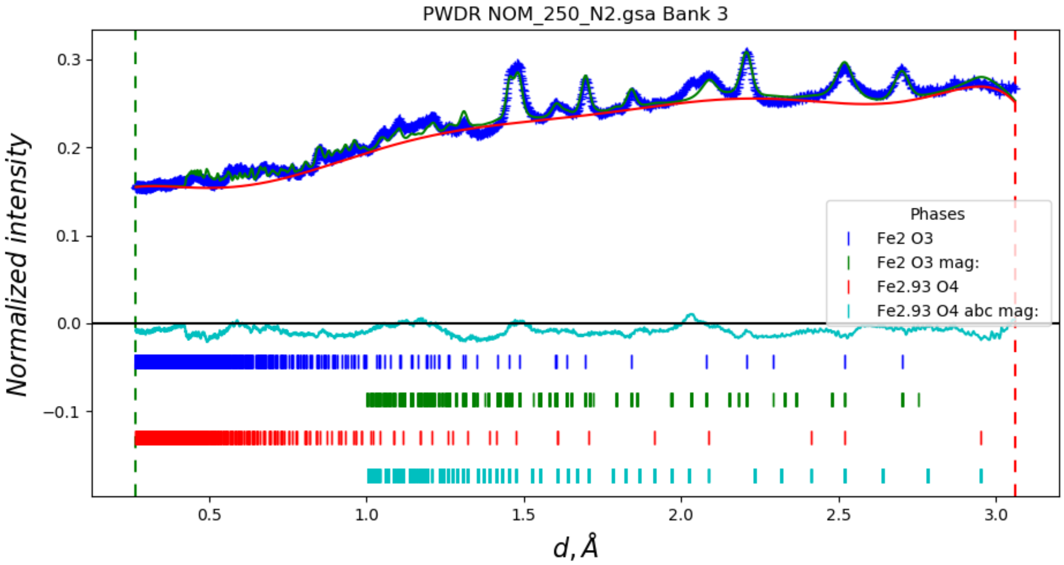

Figure S36: NOMAD bank 3 Rietveld refinement of the neutron Bragg peaks for N_2 calcined PCN-250, containing both magnetic and nuclear components.

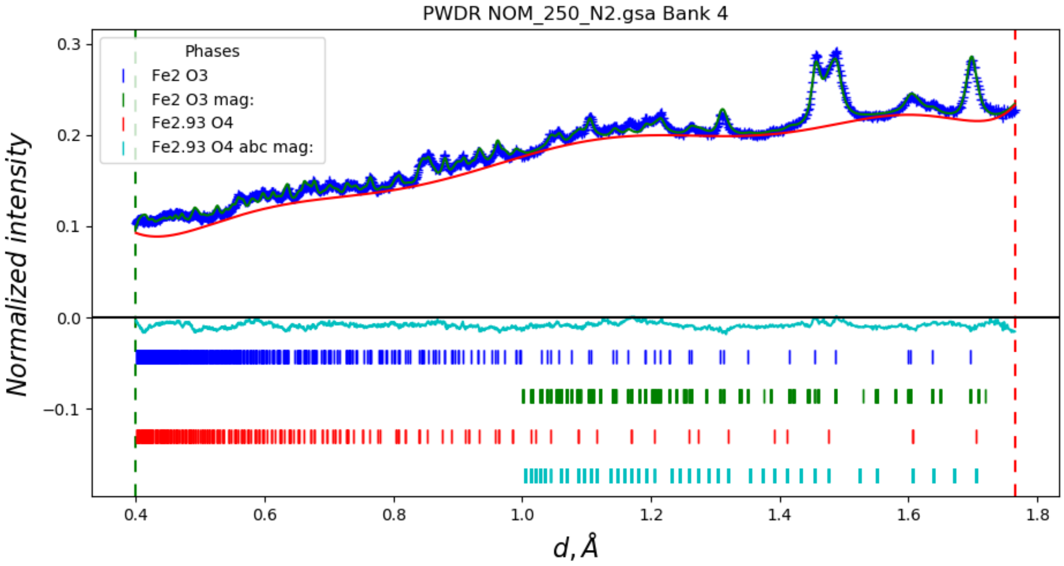

Figure S37: NOMAD bank 4 Rietveld refinement of the neutron Bragg peaks for N_2 calcined PCN-250, containing both magnetic and nuclear components.

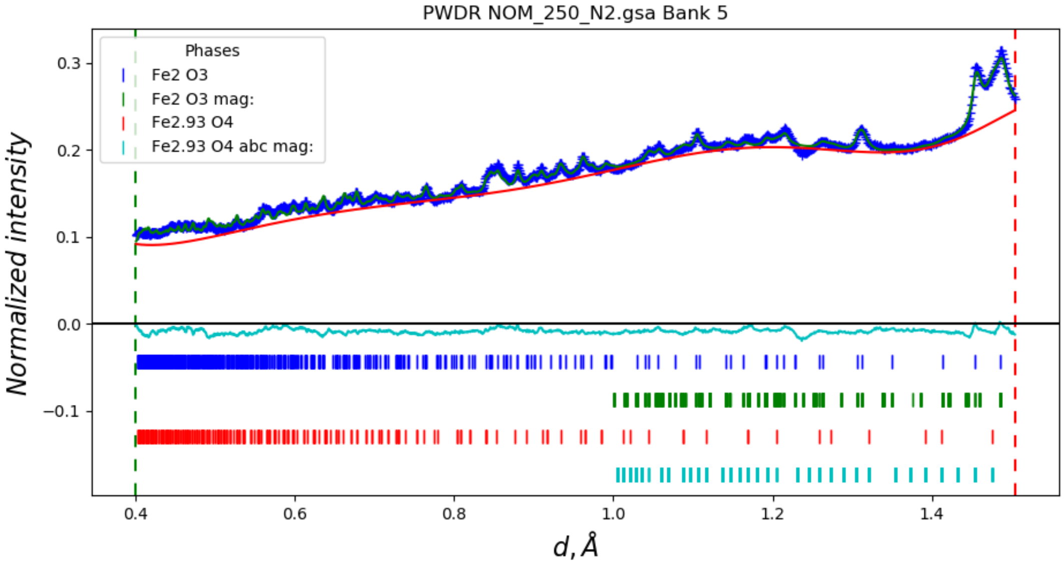

Figure S38: NOMAD bank 5 Rietveld refinement of the neutron Bragg peaks for N_2 calcined PCN-250, containing both magnetic and nuclear components.

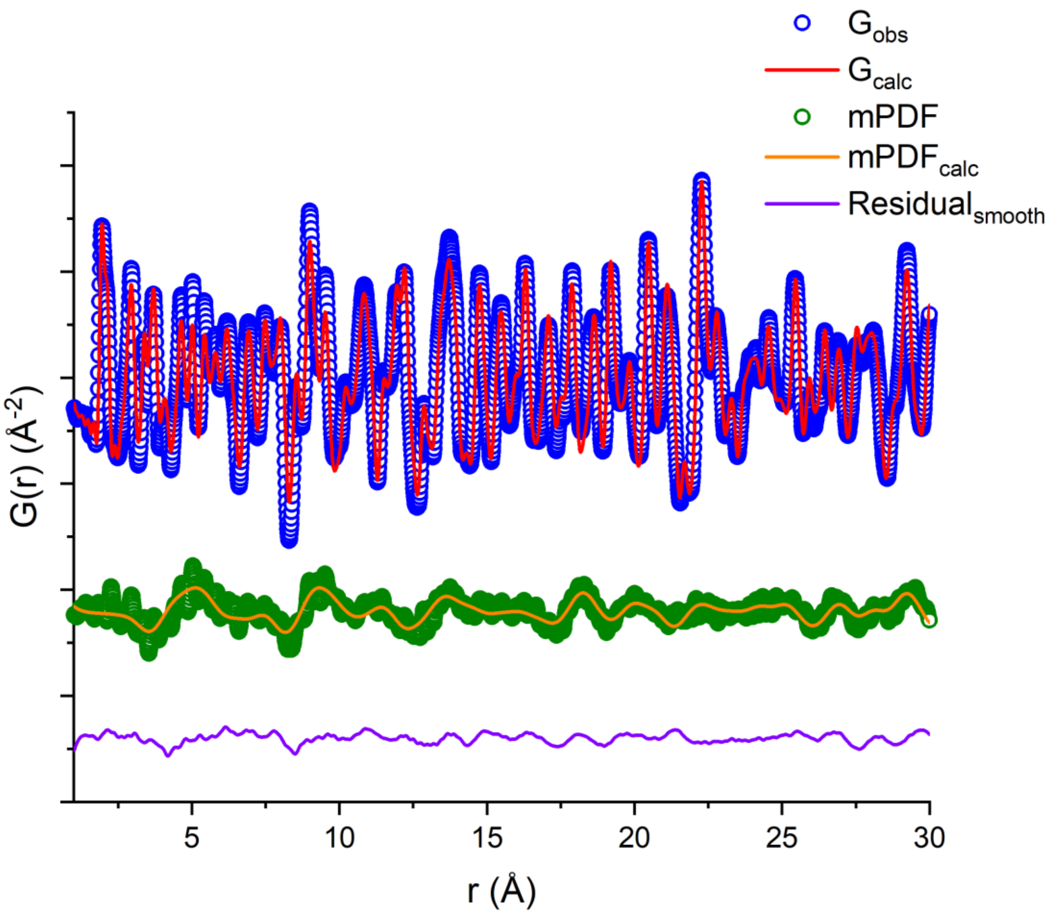

Figure S39: The total observed (blue circles) and nuclear fit (red line) of the PDF of the air calcined PCN-250, the magnetic scattering component of the PDF (green circles) was fit with the mPDF (orange line) resulting in a final residual curve (purple). The noise present in the data is removed via a 100 point 3rd order polynomial Savitzky-Golay smoothing function performed on the residual curve.

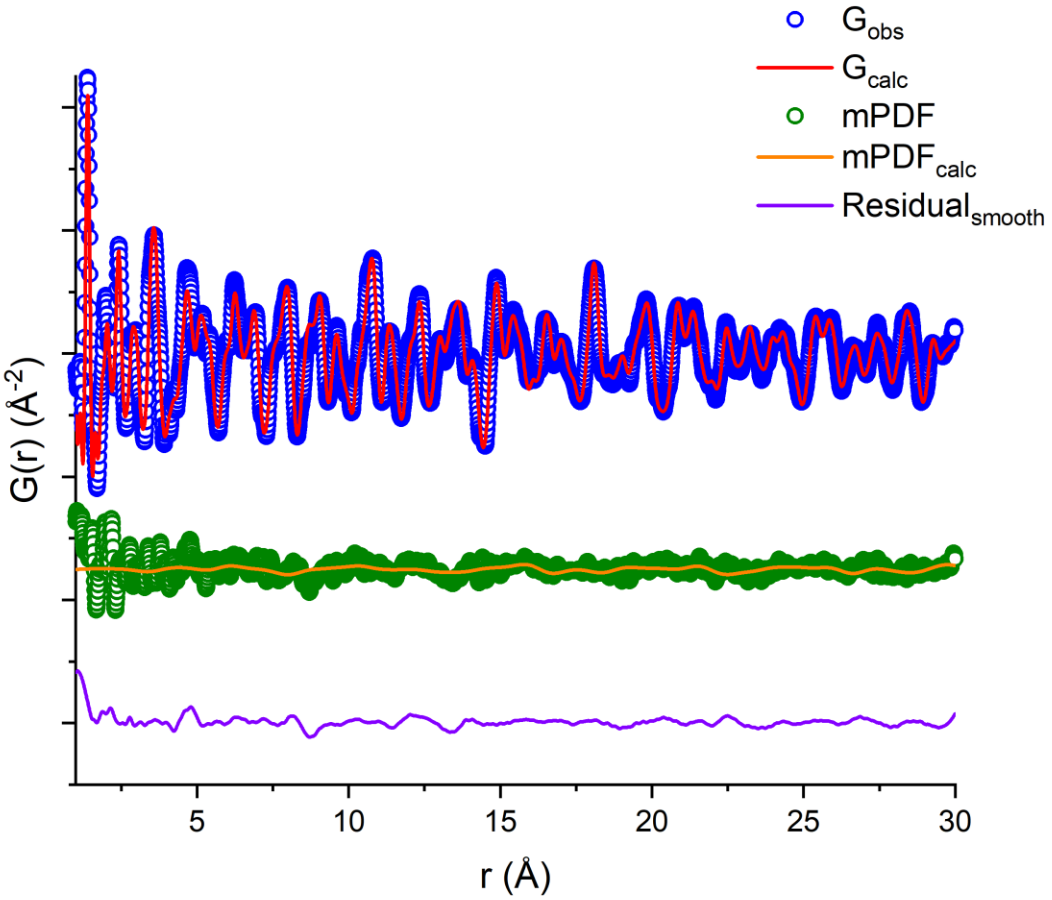

Figure S40: The total observed (blue circles) and nuclear fit (red line) of the PDF of the D_2O calcined PCN-250, the magnetic scattering component of the PDF (green circles) was fit with the mPDF (orange line) resulting in a final residual curve (purple). The noise present in the data is removed via a 100 point 3rd order polynomial Savitzky-Golay smoothing function performed on the residual curve.

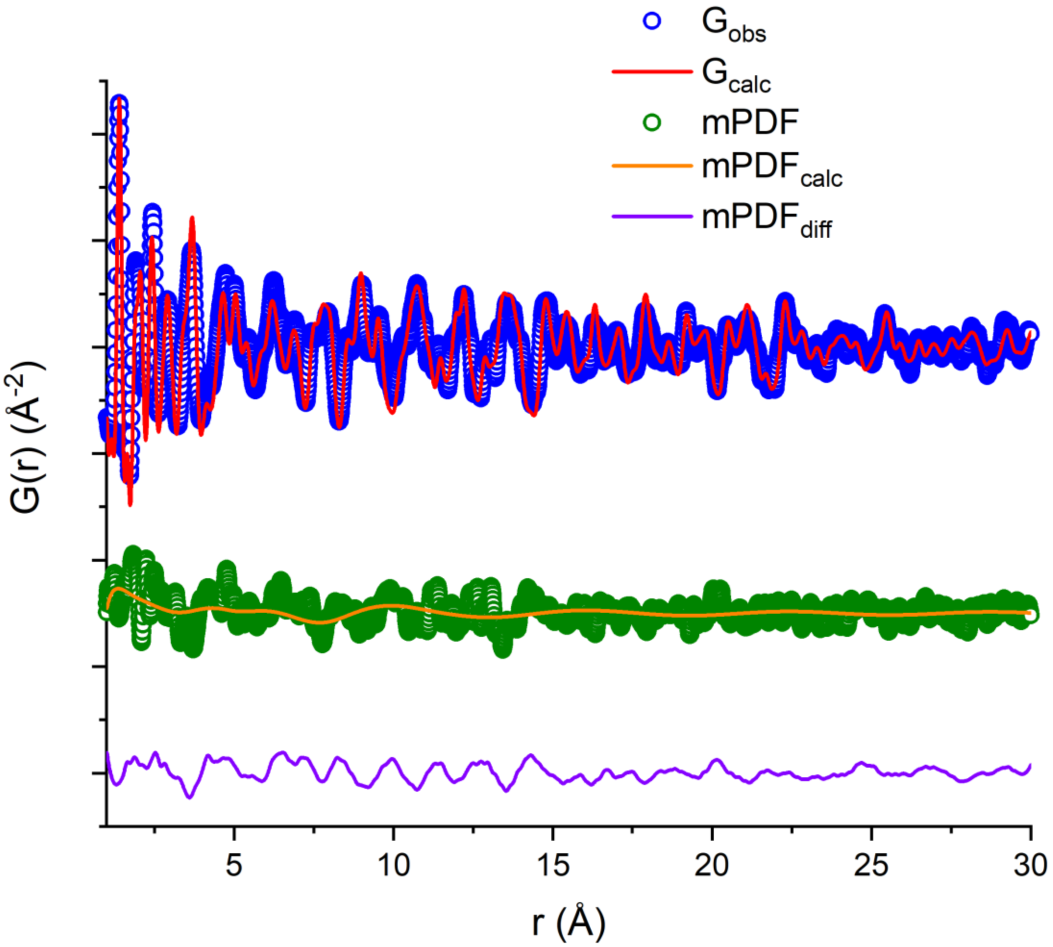

Figure S41: The total observed (blue circles) and nuclear fit (red line) of the PDF of the N_2 calcined PCN-250, the magnetic scattering component of the PDF (green circles) was fit with the mPDF (orange line) resulting in a final residual curve (purple). The noise present in the data is removed via a 100 point 3rd order polynomial Savitzky-Golay smoothing function performed on the residual curve.

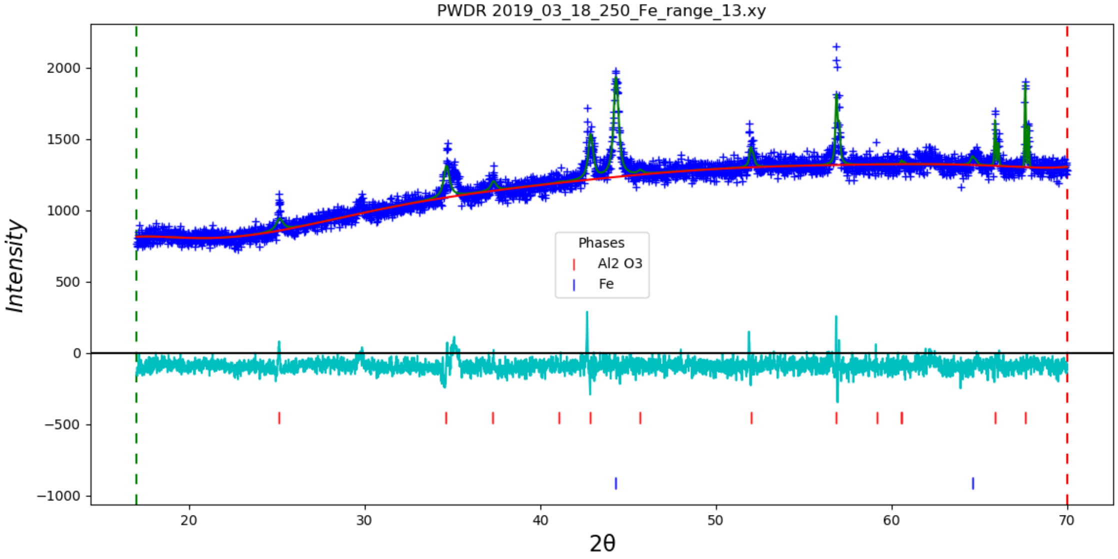

Figure S42: Post-decomposition PXRD pattern of *in situ* N_2 calcined PCN-250 modeled to zero-valent iron, the remaining peaks are from the alumina sample holder.

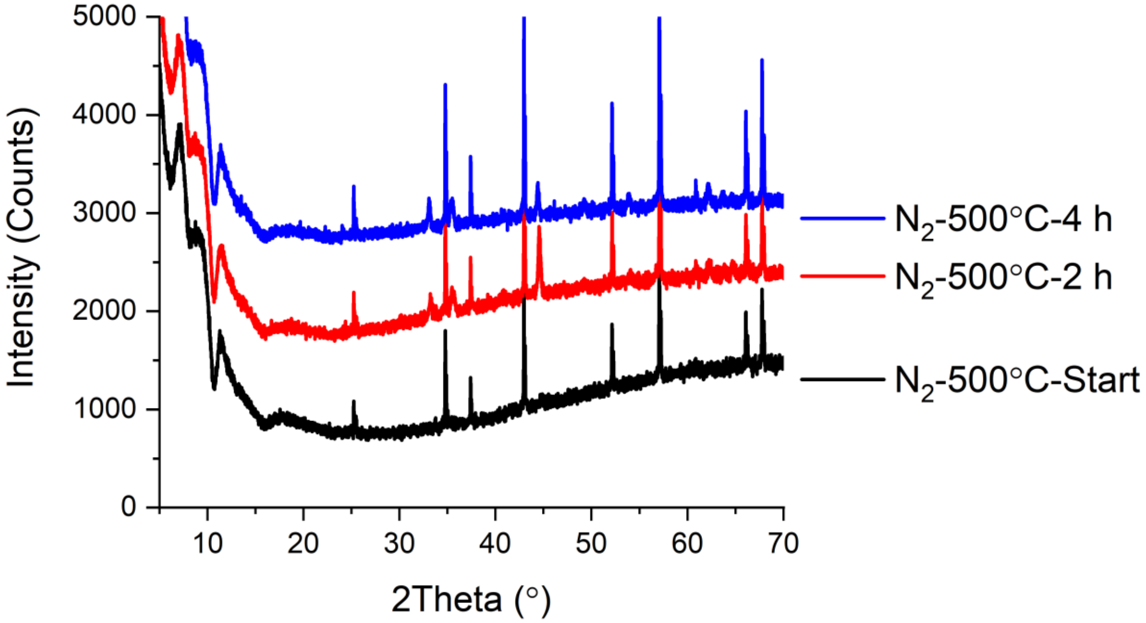

Figure S43: 4 h *in situ* PXRD of PCN-250 under N_2 held at 500 °C.

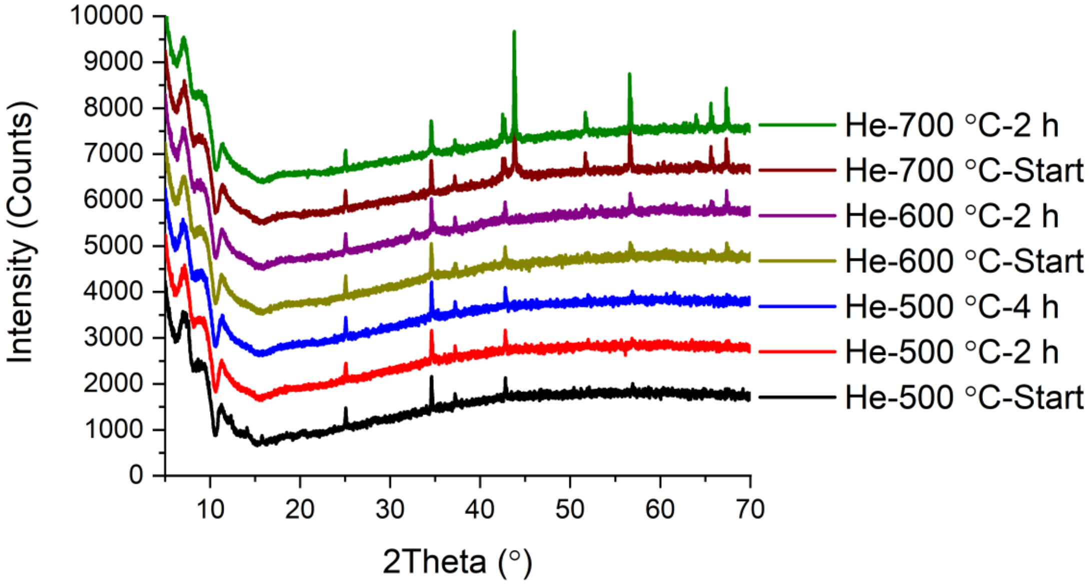

Figure S44: *In situ* PXRD of PCN-250 under He including holds at 500 °C for 4 hours, 600 °C for 2 hours, and 700 °C for 2 hours.

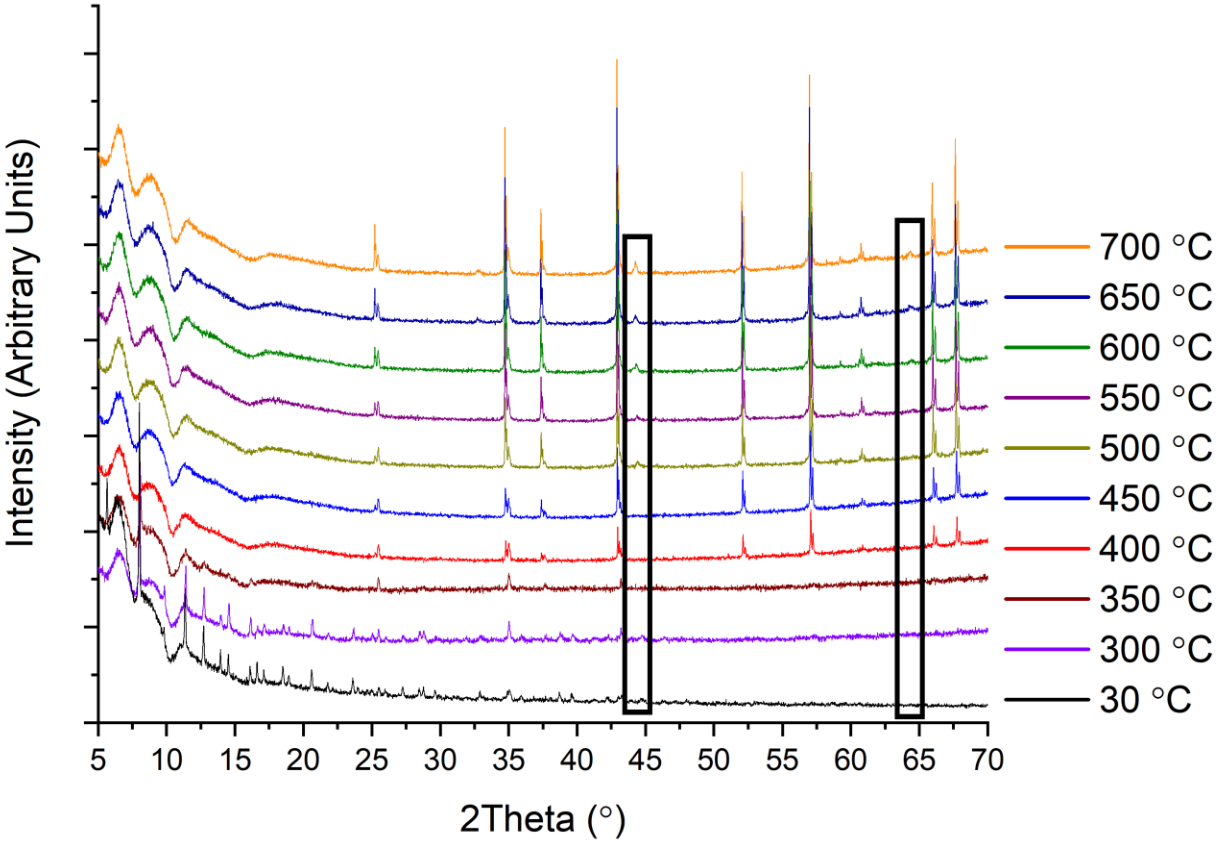

Figure S45: in situ PXRD of PCN-250 under Ar showing only small amounts of Fe(0) growth as well as peaks due to the alumina sample holder. The growth of Fe(0) appears to be less than under N_2, but higher than under He.

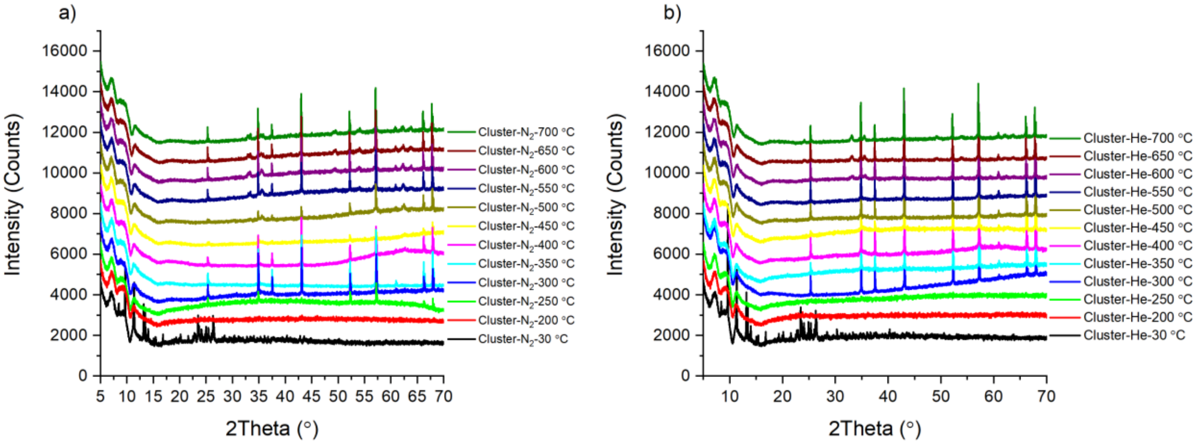

Figure S46: a) *in situ* PXRD of the calcination of the isolated $Fe_3\mu_3O$ cluster in the presence of N, b) cluster calcination in the presence of He.

Figure S47: Air free calcination set-up.

Figure S48: Air free cell for PXRD collection. The plastic dome utilized to maintain the air free atmosphere resulted in a decrease in peak intensity.

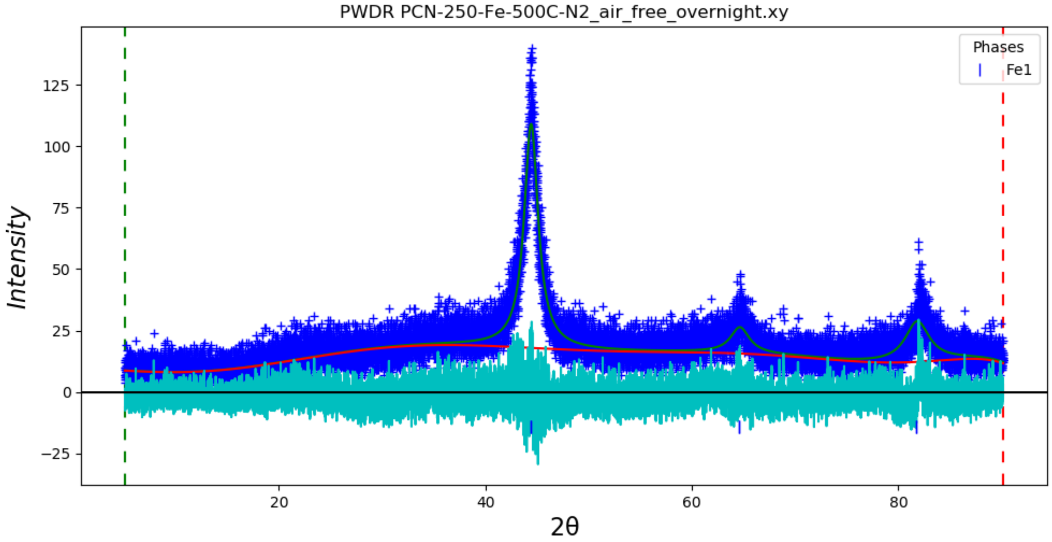

Figure S49: Air free PXRD of N_2 calcined PCN-250 collected via the air free cell and fit to zero-valent iron.

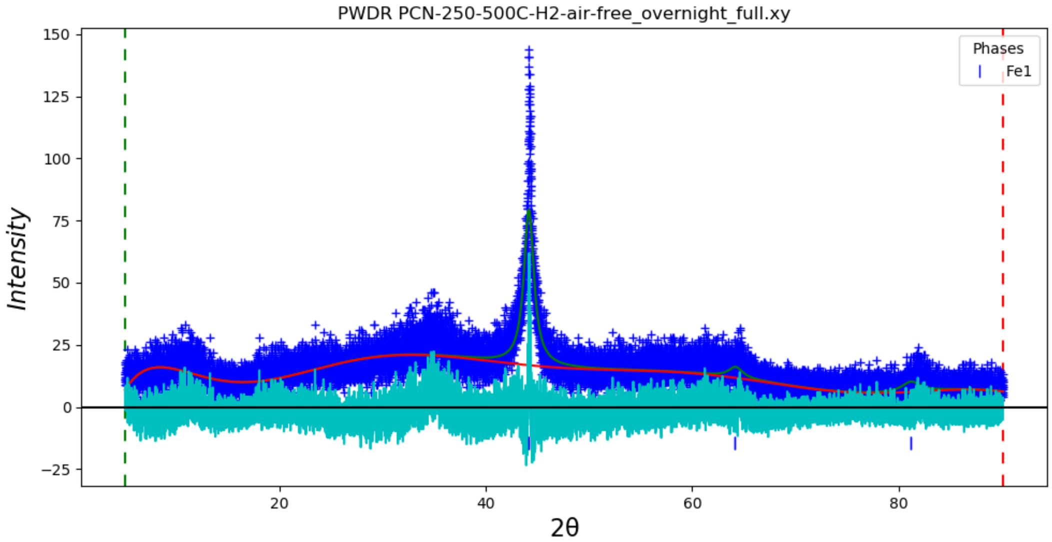

Figure S50: Air free PXRD of H_2 calcined PCN-250 collected via the air free cell and fit to zero-valent iron.

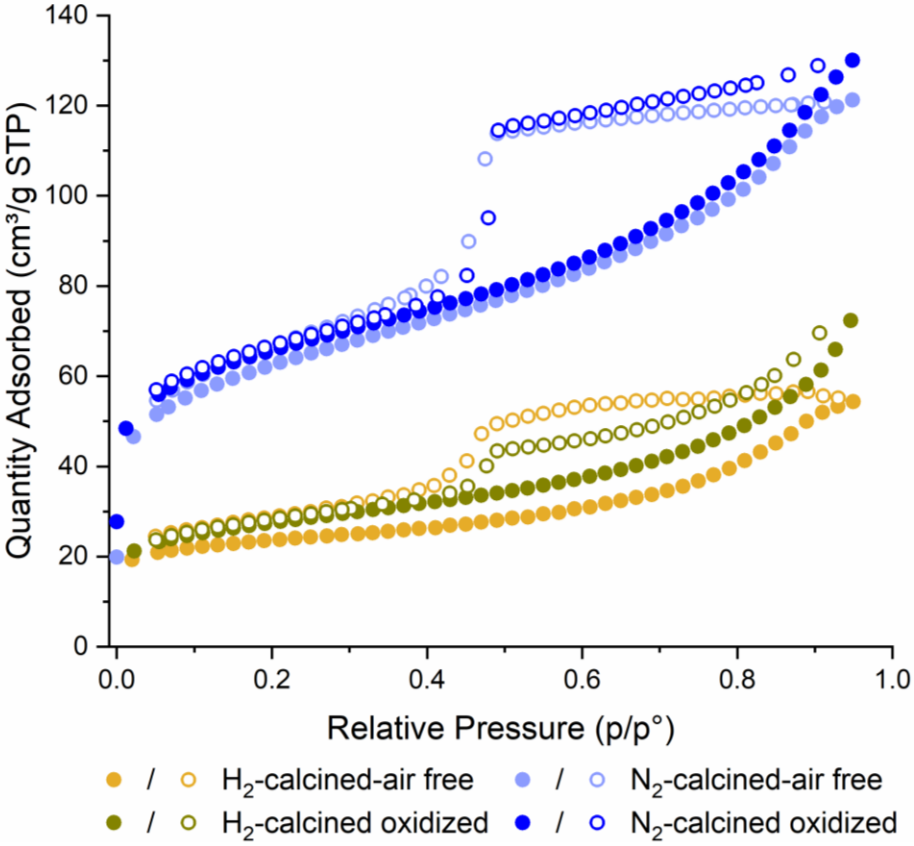

Figure S51: N_2 adsorption isotherms of the air free N_2 and H_2 calcined systems alongside samples exposed to air after calcination.

Refining Spin Angle for mPDF Calculations

As part of the mPDF systems refinement package, the angle of the spins within the structure can also be set to refine. Further refinement of the air (iron (III) oxide) and D_2O (iron (II,III) oxide) calcined samples were performed utilizing the spin angle component. The overall spin structure and the relationship between individual spins, antiferromagnetic for iron (III) oxide, and ferrimagnetic for iron (II,III) oxide) were kept for the spin angle refinement. The resulting mPDF fits (Figure S53 for air calcined in the 1-30 range, and Figure S55 for D_2O calcined in the 5-30 range), show a minimal difference in the mPDF curve before and after spin refinement. By visualizing the spin structure we can observe variation in the spin configuration of iron (III) oxide, mainly a minor increase in spin contribution in the z-direction, out of the basal plane, however, this result still largely agrees with the standard spin state model for iron (III) oxide (Figure S54). The visualized spins for iron (II,III) oxide also only differ due to a slight change in orientation in the z-direction, but otherwise maintaining the same overall spin structure (Figure S56).

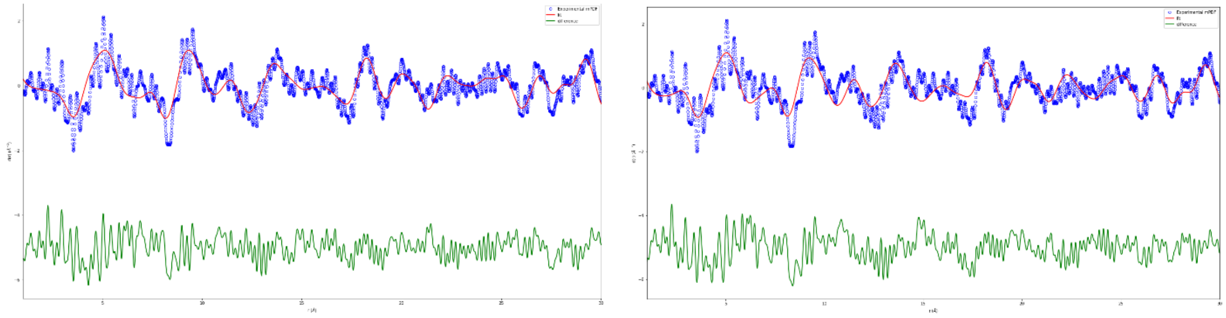

Figure S52: mPDF of the air calcined PCN-250 utilizing: left) inputted spin angles,[4] right: mPDF after refining spin angles.

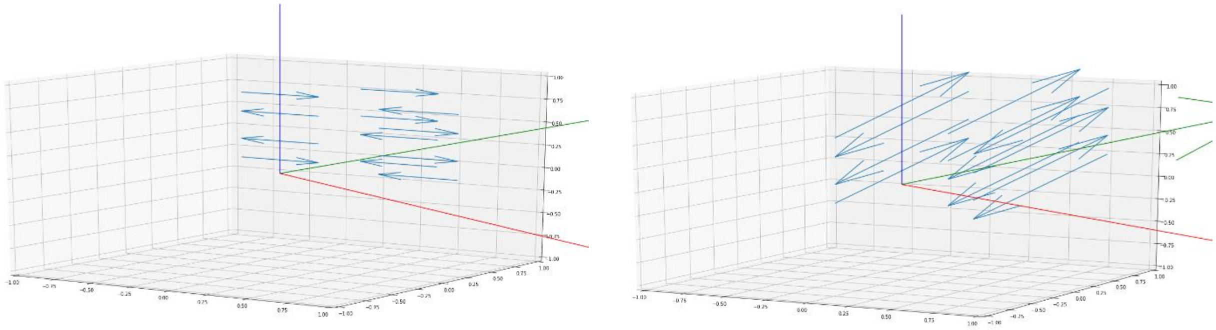

Figure S53: Visualization of the spin configuration for iron (III) oxide using left) inputted using literature spin states,[4] right) refinement of the spin angle.

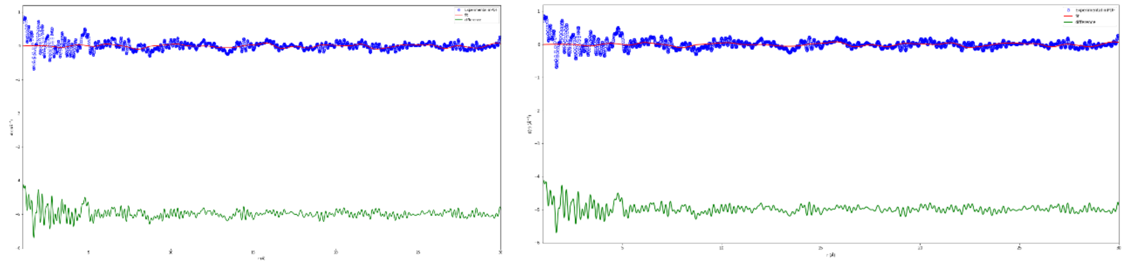

Figure S54: mPDF refinement in the 5-30 Å range for D_2O calcined PCN-250 utilizing left) a standard set of spin configuration based upon literature values,[5] right) after refining the spin angle.

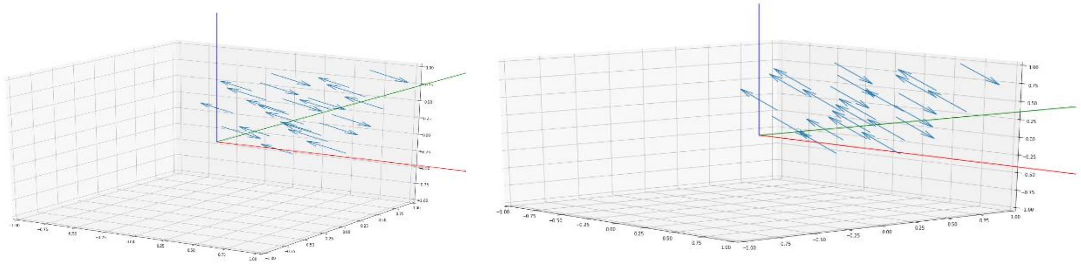

Figure S55: Spin visualization of iron (II,III) oxide utilizing left) Spin angle based on initial inputted spin configuration, right) refined spin angle.

References:

1. Neuefeind, J.; Feygenson, M.; Carruth, J.; Hoffmann, R.; Chipley, K. K., *Nuclear Instruments and Methods in Physics Research Section B: Beam Interactions with Materials and Atoms* **2012,** *287*, 68-75.
2. Toby, B. H.; Von Dreele, R. B., *Journal of Applied Crystallography* **2013,** *46* (2), 544-549.
3. Farrow, C. L.; Juhas, P.; Liu, J. W.; Bryndin, D.; Božin, E. S.; Bloch, J.; Proffen, T.; Billinge, S. J. L., *Journal of Physics: Condensed Matter* **2007,** *19* (33), 335219.
4. Hill, A. H.; Jiao, F.; Bruce, P. G.; Harrison, A.; Kockelmann, W.; Ritter, C., *Chemistry of Materials* **2008,** *20* (15), 4891-4899.
5. Banerjee, S. K.; Moskowitz, B. M., Ferrimagnetic Properties of Magnetite. In *Magnetite Biomineralization and Magnetoreception in Organisms: A New Biomagnetism*, Kirschvink, J. L.; Jones, D. S.; MacFadden, B. J., Eds. Springer US: Boston, MA, 1985; pp 17-41.